Communications on Applied Mathematics and Computation
https://doi.org/10.1007/s42967-024-00367-0

ORIGINAL PAPER

A Semi-implicit Finite Volume Scheme for Incompressible Two-Phase Flows

Davide Ferrari[1] · **Michael Dumbser**[1]

This paper is dedicated to Gerald Warnecke at the occasion of his 65th birthday and in honor of his groundbreaking scientific contributions to the field of numerical methods for the hyperbolic PDE. The authors are also very grateful for the friendship and all the inspiring discussions over the years.

Received: 26 March 2023 / Revised: 8 November 2023 / Accepted: 3 January 2024

Abstract

This paper presents a mass and momentum conservative semi-implicit finite volume (FV) scheme for complex non-hydrostatic free surface flows, interacting with moving solid obstacles. A simplified incompressible Baer-Nunziato type model is considered for two-phase flows containing a liquid phase, a solid phase, and the surrounding void. According to the so-called diffuse interface approach, the different phases and consequently the void are described by means of a scalar volume fraction function for each phase. In our numerical scheme, the dynamics of the liquid phase and the motion of the solid are decoupled. The solid is assumed to be a moving rigid body, whose motion is prescribed. Only after the advection of the solid volume fraction, the dynamics of the liquid phase is considered. As usual in semi-implicit schemes, we employ staggered Cartesian control volumes and treat the nonlinear convective terms explicitly, while the pressure terms are treated implicitly. The non-conservative products arising in the transport equation for the solid volume fraction are treated by a path-conservative approach. The resulting semi-implicit FV discretization of the mass and momentum equations leads to a mildly nonlinear system for the pressure which can be efficiently solved with a nested Newton-type technique. The time step size is only limited by the velocities of the two phases contained in the domain, and not by the gravity wave speed nor by the stiff algebraic relaxation source term, which requires an implicit discretization. The resulting semi-implicit algorithm is first validated on a set of classical incompressible Navier-Stokes test problems and later also adds a fixed and moving solid phase.

Keywords Staggered semi-implicit finite volume (FV) method · Incompressible two-phase flows · Diffuse interface approach · Incompressible free-surface Navier-Stokes equations · Violent non-hydrostatic flows · Fixed and moving solid obstacles

Mathematics Subject Classification 65M08 · 35M13 · 76T99

Extended author information available on the last page of the article

1 Introduction

Incompressible multiphase flow problems, such as the solid-liquid flows considered in this paper, are encountered in many geophysical processes, as well as in many industrial applications, for example, in the automotive industry, marine and floating technologies, and renewable energy production via water and wind turbines. These flows can be described mathematically by a Baer-Nunziato-type model for incompressible two-phase flows.

Overall, there are three different families of numerical methods for dealing with this type of problem: (i) Lagrangian and Arbitrary-Lagrangian-Eulerian (ALE) methods on moving meshes, where the free surface of the fluid and the fluid-solid interface are exactly solved by the moving computational grid, see e.g., [13, 25]; (ii) Eulerian sharp interface methods on fixed meshes with explicit interface reconstruction; (iii) Eulerian diffuse interface methods on fixed grids, where the presence of each material is represented only by a scalar function, see e.g., [23, 32, 33, 35, 37, 39] and references therein.

The method presented in this paper is an extension in terms of multi-physics of the semi-implicit mass and momentum conservative scheme for complex non-hydrostatic free surface flows presented in [18, 34]. Whereas in the previous publications, the solid phase was either completely absent or fixed, in this paper a more general method for the numerical solution of incompressible two-phase flows containing a moving liquid, a moving solid phase and void is developed. According to the so-called diffuse interface approach, the domain is covered by the liquid phase, the solid phase and by the surrounding void via a scalar volume fraction function for each phase. The diffuse interface approach allows to discretize arbitrarily complex geometries and complex free surface flows despite the fact that simple uniform Cartesian meshes are used.

Similar to [18, 34], an operator splitting is employed and the equations are discretized on a staggered Cartesian mesh, with the pressure defined in the cell centers and the velocities on the edges of the control volumes. The nonlinear convective and viscous subsystems are discretized with the aid of an explicit finite volume (FV) method, while the pressure subsystem is discretized using an FV implicit discretization over edge staggered grids. The non-conservative transport equation for the solid volume fraction is solved via the path-conservative approach of Castro et al. [16, 41]. Moreover, the algebraic velocity relaxation term may also become stiff and thus require an implicit discretization. This particular choice of implicit and explicit discretizations removes the stability condition on the gravity (pressure) wave speed and on the *stiff* relaxation source term. Thus, only a mild time step restriction, based on the velocity of the fluid and on the velocity of the moving solid bodies, is required to satisfy the Courant-Friedrichs-Lewy (CFL) stability condition.

The resulting semi-implicit FV discretization of the mass and momentum equations leads to a mildly nonlinear system for the pressure which can be efficiently solved with the nested Newton-type technique recently introduced and analyzed by Brugnano and Casulli in [9, 10].

The rest of the paper is organized as follows: first, in Sect. 2 the governing equations for the liquid and the solid phases are presented; in Sect. 3 the semi-implicit path-conservative FV scheme is described on staggered Cartesian control volumes and according to the diffuse interface approach. In Sect. 4 a thorough validation is carried out on a set of several classical benchmark problems for the incompressible Navier-Stokes equations, ranging from the Blasius boundary layer, the Hagen-Poiseuille flow, and the lid-driven cavity test to more challenging test problems for incompressible two-phase flow problems where the liquid interacts with moving solid bodies. Finally, in Sect. 5 some concluding remarks are given.

2 Governing Partial Differential Equations (PDEs)

The two-phase flows of interest in this paper can be mathematically described by a reduced Baer-Nunziato-type model for incompressible two-phase flows. The model was originally introduced for compressible two-phase flows by Baer and Nunziato in [3] and was subsequently studied and used by many authors, see e.g., [2, 27, 32, 39, 44, 45, 47] and references therein. However, in the incompressible limit it can be strongly simplified to a reduced three-equation model with an interphase velocity relaxation source term. The system of partial differential equations (PDEs) is written in terms of a solid volume fraction α^s and a liquid volume fraction α^l, according to the so-called diffuse interface approach and assuming the density as a constant $\rho = \text{const}$. It is given by the following non-conservative system of PDEs:

$$\frac{\partial \alpha^s}{\partial t} + u_k^s \frac{\partial \alpha^s}{\partial x_k} = 0, \tag{1}$$

$$\frac{\partial \alpha^l}{\partial t} + \frac{\partial (\alpha^l u_k)}{\partial x_k} = 0, \tag{2}$$

$$\frac{\partial (\alpha^l u_i)}{\partial t} + \frac{\partial (\alpha^l u_i u_k)}{\partial x_k} + \alpha^l \frac{\partial p}{\partial x_i} - \frac{\partial (\sigma_{ik})}{\partial x_k} = -\alpha^l g_i - \frac{(\alpha^s \alpha^l)^2}{\epsilon}(u_i - u_i^s), \tag{3}$$

where u_i is the velocity field of the liquid, u_i^s is the (known) velocity of the solid phase, t is the time, x_k is the spatial coordinate vector, p is the normalized pressure with respect to the constant density, $g_i = g(0,-1)^{\mathrm{T}}$ is the vector of gravity acceleration, ϵ is a time scale for the velocity relaxation kinetics, and the shear stress tensor is denoted by σ_{ik}, assuming a viscous incompressible Newtonian fluid. It is given by

$$\sigma_{ik} = \alpha^l \nu \frac{\partial u_i}{\partial x_k}, \tag{4}$$

where $\nu = \mu/\rho$ denotes the kinematic viscosity coefficient. Moreover, the liquid and the solid volume fractions α^l and α^s are related to the volume occupied respectively by the liquid V^l or by solid V^s in a control volume Ω_i by

$$V^l = \int_{\Omega_i} \alpha^l \mathrm{d}\Omega \quad \text{and} \quad V^s = \int_{\Omega_i} \alpha^s \mathrm{d}\Omega. \tag{5}$$

The *relaxation* source term, in (3), represents the mutual interactions between the two phases, describing the fact that the fluid velocity tends to the solid one at the interface of the phases, if ϵ is small enough.

The non-conservative system (1)–(3) can be expressed in an even more compact notation by defining a column vector $\mathbf{Q}$ of state variables, a flux tensor $\mathbf{F}(\mathbf{Q})$ which includes the purely conservative part of the PDE system, a so-called non-conservative product $\mathbf{B}(\mathbf{Q}) \cdot \nabla \mathbf{Q}$ and the vector of potentially stiff algebraic relaxation source terms $\mathbf{S}(\mathbf{Q})$,

$$\partial_t \mathbf{Q} + \nabla \cdot \mathbf{F}(\mathbf{Q}) + \mathbf{B}(\mathbf{Q}) \cdot \nabla \mathbf{Q} = \mathbf{S}(\mathbf{Q}). \tag{6}$$

As proposed in some recent works, in which new families of *conservative* pressure-based semi-implicit schemes were introduced on staggered Cartesian and general unstructured meshes, see e.g., [7, 12, 22, 24, 26, 31, 38, 50–52], the flux tensor is now split into a convective flux tensor $\mathbf{F}_c(\mathbf{Q})$ containing the hyperbolic part of the PDE system (1)–(3), a viscous parabolic flux tensor $\mathbf{F}_\nu(\mathbf{Q})$, and the remaining terms; hence, (6) can be rewritten as

$$\partial_t \mathbf{Q} + \nabla \cdot (\mathbf{F}_c(\mathbf{Q}) + \mathbf{F}_\nu(\mathbf{Q})) + \mathbf{B}(\mathbf{Q}) \cdot \nabla \mathbf{Q} = \mathbf{S}(\mathbf{Q}), \tag{7}$$

where the vector of state variables, the flux tensors, and the non-conservative products are given as

$$\mathbf{Q} = \begin{pmatrix} \alpha^s \\ \alpha^l \\ \alpha^l u_i \end{pmatrix}, \quad \mathbf{F}_c(\mathbf{Q}) = \begin{pmatrix} 0 \\ \alpha^l u_k \\ \alpha^l u_i u_k \end{pmatrix}, \quad \mathbf{F}_\nu(\mathbf{Q}) = \begin{pmatrix} 0 \\ 0 \\ -\alpha^l \nu \frac{\partial u_i}{\partial x_k} \end{pmatrix}, \tag{8}$$

$$\mathbf{B}(\mathbf{Q}) \cdot \nabla \mathbf{Q} = \begin{pmatrix} u^s_k \frac{\partial \alpha^s}{\partial x_k} \\ 0 \\ \alpha^l \frac{\partial p}{\partial x_k} \end{pmatrix}, \tag{9}$$

and $\mathbf{S}(\mathbf{Q})$, the algebraic source term corresponding to the right-hand side of (1)–(3), reads

$$\mathbf{S}(\mathbf{Q}) = \begin{pmatrix} 0 \\ 0 \\ -\alpha^l g e_{g_i} - \frac{1}{\epsilon}(\alpha^s)^2 \alpha^l (\alpha^l u_i - \alpha^l u^s_i) \end{pmatrix}. \tag{10}$$

This flux splitting procedure is quite useful to decouple the complete evolution system (7) into a convection-diffusion subsystem, a pressure subsystem, and an algebraic source term subsystem, which will be discretized explicitly or implicitly according to their properties. Note that, the resulting split convective fluxes represent the advection system of the flux-vector splitting scheme of Toro and Vázquez-Cendón [57] also used in [4, 14, 15].

Throughout this paper, for simplicity the two-dimensional case is considered. The computational domain is denoted by $\Omega \subset \mathbb{R}^2$ in which $x_1 = x$ and $x_2 = y$, where the x-axis is horizontal and the vertical y-axis is oriented upward against the gravity direction.

3 The Semi-implicit Finite Volume (FV) Scheme

To solve the system (7) numerically, a pressure-based staggered semi-implicit scheme is employed, similar to previous work presented in [18, 34]. To obtain a conservative semi-implicit FV scheme, first a classical operator splitting strategy is applied by decoupling the convective and pressure terms. Consequently, the weak form of each subsystem is discretized, where the non-conservative products are treated by a path-conservative approach. The previous formulation is also extended to take into account the new stiff algebraic relaxation source term in $\mathbf{S}(\mathbf{Q})$ related to the boundary condition between the two phases.

In this numerical scheme, the dynamics of the liquid phase and the solid phase motion are decoupled. By solving the solid advection equation (1), with a prescribed solid velocity field u^s_k, one obtains the new solid volume fraction distribution α^s, which is needed in the constitutive relationship of the liquid phase volume and in the relaxation source term. Furthermore, to solve the liquid phase related subsystem (7), which can be obtained from the flux splitting approach, a specific combination of explicit and implicit FV discretizations on staggered Cartesian control volumes is introduced. An implicit FV discretization of the liquid mass conservation is adopted while for the momentum equations a semi-implicit FV discretization will be employed. The convective and viscous subsystems, referred to convective and viscous fluxes $\mathbf{F}_c(\mathbf{Q})$ and $\mathbf{F}_v(\mathbf{Q})$, are discretized with the aid of an explicit FV method, thus obtaining an intermediate approximation of the conservative variables vector. The pressure subsystem, related to the purely non-conservative part of the system $\mathbf{B}(\mathbf{Q}) \cdot \nabla \mathbf{Q}$ is discretized using an implicit discretization over edge staggered grids, based on the path-conservative approach of Castro et al. [16, 41]. Moreover, the new algebraic relaxation source term, in $\mathbf{S}(\mathbf{Q})$, may also become stiff and thus require an integral implicit discretization again based on an edge staggered volume. These implicit subsystems are then coupled to the implicit liquid mass conservation law, leading to a mildly nonlinear system for the pressure. The diagonal nonlinearity of this system stems from the definition of the volume of fluid, while the remaining linear part of the system is symmetric and at least positive semi-definite. Hence, the pressure can be efficiently obtained with the family of nested Newton-type techniques introduced by Brugnano et al. in [9, 10, 20, 21].

3.1 Computational Grid and Constitutive Relationship for the Liquid Phase

Within the computational domain $\Omega \subset \mathbb{R}^2$ three staggered overlapping Cartesian control volumes are defined, a primal control volume and two staggered edge-based cells in the x- and y-directions, see e.g., [30]. Figure 1 (left) shows all three types of control volumes with their respective barycenters. The primal control volumes are

$$\Omega_{i,j} = [x_{i-\frac{1}{2}}, x_{i+\frac{1}{2}}] \times [y_{j-\frac{1}{2}}, y_{j+\frac{1}{2}}] \tag{11}$$

with the barycenters denoted by $\mathbf{x}_{i,j} = (x_i, y_j)$ and having width and height

$$\Delta x_i = x_{i+\frac{1}{2}} - x_{i-\frac{1}{2}}, \quad \Delta y_j = y_{j+\frac{1}{2}} - y_{j-\frac{1}{2}}. \tag{12}$$

The elements of the edge-based staggered mesh in the x-direction are denoted by

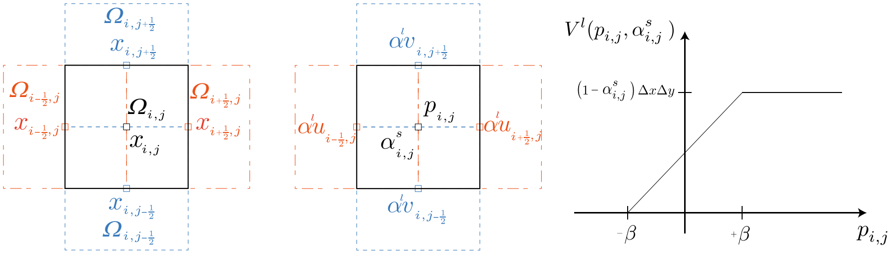

Fig. 1 Representation of the three overlapping Cartesian control volumes, in black the primal control volume, in red the elements of the edge-based staggered mesh in the x-direction, and in blue the volumes of the edge-based staggered mesh in the y-direction (left). Location of the liquid and solid phase related variables over the control volumes (center). Fluid volume is defined as a piecewise linear function of the local cell pressure $p_{i,j}$ and of the local solid phase volume fraction $\alpha^s_{i,j}$ (right)

$$\Omega_{i+\frac{1}{2},j} = [x_i, x_{i+1}] \times [y_{j-\frac{1}{2}}, y_{j+\frac{1}{2}}], \tag{13}$$

having barycenters in $\mathbf{x}_{i+\frac{1}{2},j} = (x_{i+\frac{1}{2}}, y_j)$. Their width is $\Delta x_{i+\frac{1}{2}} = x_{i+1} - x_i$ and their height is Δy_j. The volumes of the edge-based staggered mesh in the y-direction are denoted by

$$\Omega_{i,j+\frac{1}{2}} = [x_{i-\frac{1}{2}}, x_{i+\frac{1}{2}}] \times [y_j, y_{j+1}]. \tag{14}$$

Their barycenters are located in $\mathbf{x}_{i,j+\frac{1}{2}} = (x_i, y_{j+\frac{1}{2}})$ and they have width Δx_i and height $\Delta y_{j+\frac{1}{2}} = y_{j+1} - y_j$, respectively.

In the following description of the numerical method and for all the tests that will be presented, uniform Cartesian control volumes with uniform mesh spacing, at least according to each direction, are taken into account, hence $\Delta x_i = \Delta x_{i+\frac{1}{2}} = \Delta x$ and $\Delta y_j = \Delta y_{j+\frac{1}{2}} = \Delta y$. The discrete liquid phase related variables $\alpha^l u$, $\alpha^l v$, and p at a time level t^n will be defined at staggered locations, within the three introduced overlapping Cartesian control volumes, as represented in Fig. 1 (center). The discrete pressure $p^n_{i,j}$ and the liquid volume fractions $\alpha^{l,n}_{i,j}$ will be defined as cell-averaged quantities over the primal control volumes $\Omega_{i,j}$. The state variables $\alpha^l u^n_{i\pm\frac{1}{2},j}$ will be defined in the barycenters of the edge-based staggered mesh in the x-direction $\Omega_{i\pm\frac{1}{2},j}$, while the state quantity associated with the vertical components of the velocity $\alpha^l v^n_{i,j\pm\frac{1}{2}}$, will be defined in the barycenters of the edge-based staggered mesh in the y-direction $\Omega_{i,j\pm\frac{1}{2}}$.

To preserve the non-hydrostatic properties of the system of equations (7) and to relate the pressure to the volume of the liquid phase, it is necessary to introduce a closure relation. Therefore, the pressure is assumed to be linear within each cell with respect to the value in the center:

$$p(x, y, t^n) = p^n_{i,j} + g(y_j - y), \quad \forall (x, y) \in \Omega_{i,j}. \tag{15}$$

For the sake of clarity, we specify that the cell-centered pressure values, $p^n_{i,j}$, are the solution of the fully non-hydrostatic problem. The assumption of a cell-local linear pressure (15) is only needed to define the following integral of the liquid phase volume in the case of partially wet cells in such a way that the overall method reduces to a semi-implicit scheme for the shallow water equations in the special case where the fluid covers only one single layer of cells, see [17, 18] for details. Then, according to [18], the volume of the liquid phase $V^{l,n}_{i,j}$, within the cell $\Omega_{i,j}$, is related to the local cell pressure $p^n_{i,j}$ and to the solid volume fraction $\alpha^s_{i,j}$ by the following constitutive relationship:

$$V^{l,n}_{i,j} = \int_{\Omega_{i,j}} \left(1 - \alpha^{s,n}_{i,j}\right) \mathcal{H}(p^n_{i,j} + g(y_j - y)) \, \mathrm{d}x\mathrm{d}y, \tag{16}$$

defined by the Heaviside step function

$$\mathcal{H} = \begin{cases} 1, & \text{if } p^n_{i,j} + g(y_j - y) \geqslant 0, \\ 0, & \text{otherwise.} \end{cases} \tag{17}$$

Equation (16) can be more conveniently expressed in terms of a Jordan decomposition as

$$V^{l,n}_{i,j} = P(p^n_{i,j}, \alpha^{s,n}_{i,j})(p^n_{i,j} + \beta) - Q(p^n_{i,j}, \alpha^{s,n}_{i,j})(p^n_{i,j} - \beta), \tag{18}$$

where $\beta = g\frac{\Delta y}{2}$, and P and Q are step functions defined as

$$P(p^n_{i,j}, \alpha^{s,n}_{i,j}) = \begin{cases} \left(1 - \alpha^{s,n}_{i,j}\right)\frac{\Delta x}{g}, & \text{if } p^n_{i,j} \geqslant -\beta, \\ 0, & \text{otherwise} \end{cases} \tag{19}$$

and

$$Q(p^n_{i,j}, \alpha^{s,n}_{i,j}) = \begin{cases} \left(1 - \alpha^{s,n}_{i,j}\right)\frac{\Delta x}{g}, & \text{if } p^n_{i,j} > \beta, \\ 0, & \text{otherwise.} \end{cases} \tag{20}$$

The discrete solid phase volume fraction $\alpha^{s,n}_{i,j}$ and also the velocities $u^{s,n}_{i,j}$, $v^{s,n}_{i,j}$ related to this phase are defined in the centers of the cells $\Omega_{i,j}$. Moreover, for $\alpha^s_{i,j} = 1$ the corresponding cell, obviously, cannot be occupied by the liquid phase. Thus, as illustrated in Fig. 1 (right), the liquid phase volume is defined, for each cell, as a piecewise linear function of the local cell pressure $p^n_{i,j}$ and of the local solid phase volume fraction $\alpha^{s,n}_{i,j}$.

3.2 Implicit Finite Volume (FV) Discretization of the Liquid Mass Conservation

Within a two-dimensional physical domain, the liquid mass conservation equation, which is the second equation in (7), reads

$$\partial_t \alpha^l + \partial_x(\alpha^l u) + \partial_y(\alpha^l v) = 0. \tag{21}$$

The integration of this mass conservation equation (21) over the primal space-time control volume $\Omega_{i,j} = [x_{i-\frac{1}{2}}, x_{i+\frac{1}{2}}] \times [y_{j-\frac{1}{2}}, y_{j+\frac{1}{2}}] \times [t^n, t^{n+1}]$ and the use of the Gauss theorem yield

$$\begin{aligned} &\int_{x_{i-\frac{1}{2}}}^{x_{i+\frac{1}{2}}} \int_{y_{i-\frac{1}{2}}}^{y_{j+\frac{1}{2}}} \left(\alpha^l(x, y, t^{n+1}) - \alpha^l(x, y, t^n)\right)\mathrm{d}y\mathrm{d}x \\ &+ \int_{t^n}^{t^{n+1}} \int_{y_{j-\frac{1}{2}}}^{y_{j+\frac{1}{2}}} \left(\alpha^l u(x_{i+\frac{1}{2}}, y, t) - \alpha^l u(x_{i-\frac{1}{2}}, y, t)\right)\mathrm{d}y\mathrm{d}t \\ &+ \int_{t^n}^{t^{n+1}} \int_{x_{i-\frac{1}{2}}}^{x_{i+\frac{1}{2}}} \left(\alpha^l v(x, y_{j+\frac{1}{2}}, t) - \alpha^l v(x, y_{j-\frac{1}{2}}, t)\right)\mathrm{d}x\mathrm{d}t = 0. \end{aligned} \tag{22}$$

With the definitions of the liquid cell volume

$$V^l_{i,j} = \int_{x_{i-\frac{1}{2}}}^{x_{i+\frac{1}{2}}} \int_{y_{j-\frac{1}{2}}}^{y_{j+\frac{1}{2}}} \alpha^l(x, y, t)\mathrm{d}y\mathrm{d}x, \tag{23}$$

and the liquid fluxes

$$f^l_{i+\frac{1}{2},j} = \frac{1}{\Delta t \Delta y} \int_{t^n}^{t^{n+1}} \int_{y_{j-\frac{1}{2}}}^{y_{j+\frac{1}{2}}} \alpha^l u(x_{i+\frac{1}{2}}, y, t)\mathrm{d}y\mathrm{d}t, \tag{24}$$

and

$$g^l_{i,j+\frac{1}{2}} = \frac{1}{\Delta t \Delta x}\int_{t^n}^{t^{n+1}}\int_{x_{i-\frac{1}{2}}}^{x_{i+\frac{1}{2}}} \alpha^l v(x, y_{j+\frac{1}{2}}, t)\mathrm{d}x\mathrm{d}t, \tag{25}$$

the following integral form of (21) is obtained:

$$V^{l,n+1}_{i,j} = V^{l,n}_{i,j} - \Delta t \Delta y\left(f^l_{i+\frac{1}{2},j} - f^l_{i-\frac{1}{2},j}\right) - \Delta t \Delta x\left(g^l_{i,j+\frac{1}{2}} - g^l_{i,j-\frac{1}{2}}\right). \tag{26}$$

Introducing the liquid cell-average of the liquid volume fraction

$$\alpha^l_{i,j} = \frac{1}{\Delta x \Delta y}\int_{x_{i-\frac{1}{2}}}^{x_{i+\frac{1}{2}}}\int_{y_{j-\frac{1}{2}}}^{y_{j+\frac{1}{2}}} \alpha^l(x, y, t)\mathrm{d}y\mathrm{d}x, \tag{27}$$

it is possible to rewrite (28) as

$$\alpha^{l,n+1}_{i,j} = \alpha^{l,n}_{i,j} - \frac{\Delta t}{\Delta x}\left(f^l_{i+\frac{1}{2},j} - f^l_{i-\frac{1}{2},j}\right) - \frac{\Delta t}{\Delta y}\left(g^l_{i,j+\frac{1}{2}} - g^l_{i,j-\frac{1}{2}}\right), \tag{28}$$

which is a discrete form of (21). Assuming the liquid velocity field constant along each edge, denoting these velocities at the new time t^{n+1} by $u^{l,n+1}_{i+\frac{1}{2},j}$ and $v^{l,n+1}_{i,j+\frac{1}{2}}$, and defining the effective edge lengths which are occupied by the liquid as

$$\delta y^{n+1}_{i+\frac{1}{2},j} = \int_{y_{j-\frac{1}{2}}}^{y_{j+\frac{1}{2}}} \alpha^l(x_{i+\frac{1}{2}}, y, t^{n+1})\mathrm{d}y, \quad \delta x^{n+1}_{i,j+\frac{1}{2}} = \int_{x_{i-\frac{1}{2}}}^{x_{i+\frac{1}{2}}} \alpha^l(x, y_{j+\frac{1}{2}}, t^{n+1})\mathrm{d}x, \tag{29}$$

it is possible to define the following edge-averaged liquid volume fractions:

$$\alpha^{l,n+1}_{i+\frac{1}{2},j} = \frac{\delta y^{n+1}_{i+\frac{1}{2},j}}{\Delta y} \quad \text{and} \quad \alpha^{l,n+1}_{i,j+\frac{1}{2}} = \frac{\delta x^{n+1}_{i,j+\frac{1}{2}}}{\Delta x}. \tag{30}$$

Defining the liquid fluxes in terms of the edge velocities and the edge-averaged volume fractions as

$$f^l_{i+\frac{1}{2},j} = \alpha^{l,n+1}_{i+\frac{1}{2},j}\, u^{n+1}_{i+\frac{1}{2},j} \quad \text{and} \quad g^l_{i,j+\frac{1}{2}} = \alpha^{l,n+1}_{i,j+\frac{1}{2}}\, v^{n+1}_{i,j+\frac{1}{2}}, \tag{31}$$

the liquid volume conservation equation (28) can finally be written as

$$V^{l,n+1}_{i,j} = V^{l,n}_{i,j} - \Delta t\left((\delta y u)^{n+1}_{i+\frac{1}{2},j} - (\delta y u)^{n+1}_{i-\frac{1}{2},j}\right) - \Delta t\left((\delta x v)^{n+1}_{i,j+\frac{1}{2}} - (\delta x v)^{n+1}_{i,j-\frac{1}{2}}\right). \tag{32}$$

Equation (32) represents an implicit FV discretization of the continuity equation, as the semi-implicit method proposed in [18]. The effective edge-integrated volume fractions $\delta y^{n+1}_{i+\frac{1}{2},j}$ and $\delta x^{n+1}_{i,j+\frac{1}{2}}$, available to liquid phase through the edges, can be evaluated from the liquid volumes within the cells that share the edge by taking the average, the upwind, or the maximum cell volumes. For instance, if the average is chosen, then $\delta y^{n+1}_{i+\frac{1}{2},j}$ and $\delta x^{n+1}_{i,j+\frac{1}{2}}$ read

$$\begin{aligned}\delta y^{n+1}_{i+\frac{1}{2},j} =&\Delta y\frac{1}{2}\left(\alpha^l(p^{n+1}_{i,j}) + \alpha^l(p^{n+1}_{i+1,j})\right)\\ =&\frac{1}{2\Delta x}\left(V^l(p^{n+1}_{i,j}, \alpha^{s,n+1}_{i,j}) + V^l(p^{n+1}_{i+1,j}, \alpha^{s,n+1}_{i+1,j})\right),\end{aligned} \tag{33}$$

$$\begin{aligned}\delta x^{n+1}_{i,j+\frac{1}{2}} =&\Delta x\frac{1}{2}\left(\alpha^l(p^{n+1}_{i,j}) + \alpha^l(p^{n+1}_{i,j+1})\right)\\ =&\frac{1}{2\Delta y}\left(V^l(p^{n+1}_{i,j}, \alpha^{s,n+1}_{i,j}) + V^l(p^{n+1}_{i,j+1}, \alpha^{s,n+1}_{i,j+1})\right),\end{aligned} \tag{34}$$

using for the liquid cell volume V^l the constitutive relationship defined in (18).

3.3 Semi-implicit Finite Volume (FV) Discretization of the Momentum Equations

As mentioned above the system (7) is discretized with the aid of a specific combination of explicit and implicit FV methods on staggered Cartesian control volumes to solve the subsystems which can be obtained from the flux splitting tensor introduced in the previous section.

The convective and viscous subsystems, which can be obtained considering convective and viscous fluxes $\mathbf{F}_c(\mathbf{Q})$ and $\mathbf{F}_v(\mathbf{Q})$, are discretized with an explicit FV method, and an intermediate approximation of the state variables is thus achieved. This intermediate approximation will be denoted by the super-index, e.g., $(\delta yu)^*_{i\pm\frac{1}{2},j}$ and $(\delta xv)^*_{i,j\pm\frac{1}{2}}$ which will denote the intermediate approximation of the conservative liquid fluxes expressed by the effective edge-integrated volume fractions.

Explicit discretization of the convective terms The convective, hyperbolic subsystem, which has to be discretized explicitly, reads

$$\begin{cases}\dfrac{\partial\alpha^s}{\partial t} + u^s_k\dfrac{\partial\alpha^s}{\partial x_k} = 0,\\ \dfrac{\partial(\alpha^l u_i)}{\partial t} + \dfrac{\partial(\alpha^l u_i u_k)}{\partial x_k} = 0.\end{cases} \tag{35}$$

It contains a conservative and a non-conservative part. It is useful to integrate this subsystem on the main grid to have a classical Godunov-type FV scheme, in which all state variables are defined at the centre of the cells. Starting from the known solution $\mathbf{Q}^n_{i,j}$ at time t^n, the integration of this subsystem (35) over the primal space-time control volume $\Omega_{i,j} \times [t^n, t^{n+1}]$ yields

$$\begin{aligned}\mathbf{Q}^*_{i,j} =&\mathbf{Q}^n_{i,j} - \frac{\Delta t}{\Delta x}\left(\mathbf{f}^c_{i+\frac{1}{2},j} - \mathbf{f}^c_{i-\frac{1}{2},j}\right) - \frac{\Delta t}{\Delta y}\left(\mathbf{g}^c_{i,j+\frac{1}{2}} - \mathbf{g}^c_{i,j-\frac{1}{2}}\right)\\ &- \frac{\Delta t}{\Delta x}\left(\mathbf{D}^c_{i+\frac{1}{2},j} + \mathbf{D}^c_{i-\frac{1}{2},j}\right) - \frac{\Delta t}{\Delta y}\left(\mathbf{D}^c_{i,j+\frac{1}{2}} + \mathbf{D}^c_{i,j-\frac{1}{2}}\right).\end{aligned} \tag{36}$$

Since the velocity components $u^n_{i\pm\frac{1}{2},j}$, $v^n_{i,j\pm\frac{1}{2}}$ and the previous fluxes $(\delta yu)^{n+1}_{i\pm\frac{1}{2},j}$ and $(\delta xv)^{n+1}_{i,j\pm\frac{1}{2}}$ in the discrete liquid volume conservation equation (32) are defined over the edges of the primal control volumes, an interpolation of the velocity field or fluxes from one mesh to another is needed. This interpolation, to evaluate centered fluxes on the primal control volumes, is achieved as follows:

$$(\delta yu)^n_{i,j} = \frac{1}{2}\left((\delta yu)^n_{i+\frac{1}{2},j} + (\delta yu)^n_{i-\frac{1}{2},j} \right) \tag{37}$$

and

$$(\delta xv)^n_{i,j} = \frac{1}{2}\left((\delta xv)^n_{i,j+\frac{1}{2}} + (\delta xv)^n_{i,j-\frac{1}{2}} \right), \tag{38}$$

and an average of the same type can be used to return to staggered values on the edges of the primal control volumes.

Moreover, to complete the FV scheme (36) the numerical fluxes and path-conservative jump terms have to be defined. Here, a Rusanov-type flux is chosen in the x- and y-directions and is defined as

$$\mathbf{f}^c_{i+\frac{1}{2},j} = \frac{1}{2}\left(\mathbf{f}^c(\mathbf{Q}^-_{i+\frac{1}{2},j}) + \mathbf{f}^c(\mathbf{Q}^+_{i+\frac{1}{2},j}) \right) - \frac{1}{2}|s^x_{\max}|\left(\mathbf{Q}^+_{i+\frac{1}{2},j} - \mathbf{Q}^-_{i+\frac{1}{2},j} \right) \tag{39}$$

and

$$\mathbf{g}^c_{i,j+\frac{1}{2}} = \frac{1}{2}\left(\mathbf{g}^c(\mathbf{Q}^-_{i,j+\frac{1}{2}}) + \mathbf{g}^c(\mathbf{Q}^+_{i,j+\frac{1}{2}}) \right) - \frac{1}{2}|s^y_{\max}|\left(\mathbf{Q}^+_{i,j+\frac{1}{2}} - \mathbf{Q}^-_{i,j+\frac{1}{2}} \right), \tag{40}$$

where the maximum signal speeds $s^x_{\max}$ and $s^y_{\max}$ are computed as the maxima of the eigenvalues of the explicit convective subsystem in x- and y-directions, respectively. The path-conservative jump terms [16, 41] read

$$\mathbf{D}^c_{i+\frac{1}{2},j} = \frac{1}{2}\mathbf{B}^{c,x}(\tilde{\mathbf{Q}}_{i+\frac{1}{2},j})\left(\mathbf{Q}^+_{i+\frac{1}{2},j} - \mathbf{Q}^-_{i+\frac{1}{2},j} \right), \tag{41}$$

$$\mathbf{D}^c_{i,j+\frac{1}{2}} = \frac{1}{2}\mathbf{B}^{c,y}(\tilde{\mathbf{Q}}_{i,j+\frac{1}{2}})\left(\mathbf{Q}^+_{i,j+\frac{1}{2}} - \mathbf{Q}^-_{i,j+\frac{1}{2}} \right) \tag{42}$$

with $\tilde{\mathbf{Q}}_{i+\frac{1}{2},j} = \frac{1}{2}(\mathbf{Q}^+_{i+\frac{1}{2},j} + \mathbf{Q}^-_{i+\frac{1}{2},j})$, $\tilde{\mathbf{Q}}_{i,j+\frac{1}{2}} = \frac{1}{2}(\mathbf{Q}^+_{i,j+\frac{1}{2}} + \mathbf{Q}^-_{i,j+\frac{1}{2}})$, and

$$\mathbf{B}^{c,x}(\mathbf{Q}) = \begin{pmatrix} u^s_1 & 0 & 0 \\ 0 & 0 & 0 \\ 0 & 0 & 0 \end{pmatrix}, \quad \mathbf{B}^{c,y}(\mathbf{Q}) = \begin{pmatrix} u^s_2 & 0 & 0 \\ 0 & 0 & 0 \\ 0 & 0 & 0 \end{pmatrix}. \tag{43}$$

Furthermore, to reach second order of accuracy the boundary-extrapolated and time-evolved values are computed via a standard total variation diminishing (TVD) MUSCL-Hancock scheme as follows:

$$\mathbf{Q}^{\mp}_{i+\frac{1}{2},j} = \mathbf{Q}^n_{i,j} \pm \frac{1}{2}\Delta x \partial_x \mathbf{Q}^n_{i,j} + \frac{1}{2}\Delta t \partial_t \mathbf{Q}^n_{i,j}, \tag{44}$$

$$\mathbf{Q}^{\mp}_{i,j+\frac{1}{2}} = \mathbf{Q}^n_{i,j} \pm \frac{1}{2}\Delta y \partial_y \mathbf{Q}^n_{i,j} + \frac{1}{2}\Delta t \partial_t \mathbf{Q}^n_{i,j} \tag{45}$$

with the gradient in space approximated using the classical *minmod* slope limiter

$$\partial_x \mathbf{Q}^n_{i,j} = \text{minmod}\left(\frac{\mathbf{Q}^n_{i+1,j} - \mathbf{Q}^n_{i,j}}{\Delta x}, \frac{\mathbf{Q}^n_{i,j} - \mathbf{Q}^n_{i-1,j}}{\Delta x} \right), \tag{46}$$

$$\partial_y \mathbf{Q}^n_{i,j} = \text{minmod}\left(\frac{\mathbf{Q}^n_{i,j+1} - \mathbf{Q}^n_{i,j}}{\Delta y}, \frac{\mathbf{Q}^n_{i,j} - \mathbf{Q}^n_{i,j-1}}{\Delta y} \right), \tag{47}$$

while the derivative in time is computed as

$$\begin{aligned} \partial_t \mathbf{Q}^n_{i,j} = &- \frac{\mathbf{f}^c(\mathbf{Q}^n_{i,j} + \frac{1}{2}\Delta x \partial_x \mathbf{Q}^n_{i,j}) - \mathbf{f}^c(\mathbf{Q}^n_{i,j} - \frac{1}{2}\Delta x \partial_x \mathbf{Q}^n_{i,j})}{\Delta x} \\ &- \frac{\mathbf{g}^c(\mathbf{Q}^n_{i,j} + \frac{1}{2}\Delta y \partial_y \mathbf{Q}^n_{i,j}) - \mathbf{g}^c(\mathbf{Q}^n_{i,j} - \frac{1}{2}\Delta y \partial_y \mathbf{Q}^n_{i,j})}{\Delta y} \\ &- \mathbf{B}^{c,x}\left(\mathbf{Q}^n_{i,j}\right)\partial_x \mathbf{Q}^n_{i,j} - \mathbf{B}^{c,y}\left(\mathbf{Q}^n_{i,j}\right)\partial_y \mathbf{Q}^n_{i,j}, \end{aligned} \tag{48}$$

see the Toro textbook [56] for details. From this explicit FV scheme the intermediate solution $\mathbf{Q}^*_{i,j} = ((\delta yu)^*_{i,j}, (\delta xv)^*_{i,j})^{\mathrm{T}}$ will be obtained, and from this average values on the primal control volume it is possible to go back to staggered values on the edges by interpolation obtaining $(\delta yu)^*_{i+\frac{1}{2},j}, (\delta xv)^*_{i,j+\frac{1}{2}}$.

Explicit discretization of the viscous terms The parabolic viscous subsystem, which will be also discretized explicitly, reads

$$\partial_t \mathbf{Q} + \nabla \cdot (\mathbf{F}_v(\mathbf{Q})) = 0, \tag{49}$$

where the viscous fluxes can be written as $\mathbf{F}_v(\mathbf{Q}) = (\mathbf{f}^v(\mathbf{Q}), \mathbf{g}^v(\mathbf{Q}))^{\mathrm{T}}$. The two equations which constitute the viscous subsystem (49) have to be discretized over two different staggered edge-based cells in the x- and y-directions, respectively. Indeed, at time t^n, the velocities $u^n_{i\pm\frac{1}{2},j}, v^n_{i,j\pm\frac{1}{2}}$ and the effective edge-integrated volume fractions $(\delta y)^n_{i\pm\frac{1}{2},j}, (\delta x)^n_{i,j\pm\frac{1}{2}}$ are known at staggered locations, over the edges of the primal control volumes. Therefore, to evaluate a second intermediate state $(\delta yu)^{**}_{i+\frac{1}{2},j}$ which considers also the viscous terms, the first equation in the x-direction has to be considered and integrated over the edge-based staggered space-time control volume $\Omega_{i+\frac{1}{2},j} = [x_i, x_{i+1}] \times [y_{j-\frac{1}{2}}, y_{j+\frac{1}{2}}] \times [t^n, t^{**}]$; it reads

$$(\alpha u)^{**}_{i+\frac{1}{2},j} = (\alpha u)^*_{i+\frac{1}{2},j} + \frac{\Delta t}{\Delta x}\left(f^v_{i+1,j} - f^v_{i,j}\right) + \frac{\Delta t}{\Delta y}\left(g^v_{i+\frac{1}{2},j+\frac{1}{2}} - g^v_{i+\frac{1}{2},j-\frac{1}{2}}\right) \tag{50}$$

with the definitions

$$(\alpha u)^{**}_{i+\frac{1}{2},j} = \frac{1}{\Delta x \Delta y} \int_{x_i}^{x_{i+1}} \int_{y_{j-\frac{1}{2}}}^{y_{j+\frac{1}{2}}} \alpha^l u(x,y,t^n)\mathrm{d}x\mathrm{d}y, \tag{51}$$

$$f^v_{i+1,j} = \frac{1}{\Delta t \Delta y} \int_{t^n}^{t^{n+1}} \int_{y_{j-\frac{1}{2}}}^{y_{j+\frac{1}{2}}} f^v_{(x_{i+1},y,t)}\mathrm{d}y\mathrm{d}t, \tag{52}$$

and

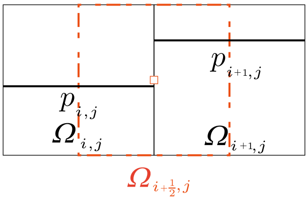

Fig. 2 Representation of the discrete states over the different staggered control volumes, in black the primal control volumes, in red the element of the edge-based staggered mesh in the x-direction over which the pressure subsystem is integrated

$$g^{\nu}_{i+\frac{1}{2},j+\frac{1}{2}} = \frac{1}{\Delta t \Delta x}\int_{t^n}^{t^{n+1}}\int_{x_i}^{x_{i+1}} g^{\nu}_{(x,y_{j+\frac{1}{2}},t)}\,\mathrm{d}x\mathrm{d}t. \tag{53}$$

As before, the liquid cell-average flux in the x-direction $(\alpha u)^{**}_{i+\frac{1}{2},j}$ can be expressed by the effective edge-integrated volume fraction $(\delta y)^{**}_{i+\frac{1}{2},j}$ as follows:

$$(\delta y u)^{**}_{i+\frac{1}{2},j} = (\alpha u)^{**}_{i+\frac{1}{2},j}\Delta y = \frac{1}{\Delta x}\int_{x_i}^{x_{i+1}}\int_{y_{j-\frac{1}{2}}}^{y_{j+\frac{1}{2}}} \alpha^l u(x,y,t^n)\,\mathrm{d}x\mathrm{d}y, \tag{54}$$

and assuming constant fluxes along each edge, it is possible to rewrite the discrete equation (50) in terms of effective volume fractions

$$(\delta y u)^{**}_{i+\frac{1}{2},j} = (\delta y u)^{*}_{i+\frac{1}{2},j} + \frac{\Delta t}{\Delta x}\left(f^{\nu}_{i+1,j} - f^{\nu}_{i,j}\right) + \frac{\Delta t}{\Delta y}\left(g^{\nu}_{i+\frac{1}{2},j+\frac{1}{2}} - g^{\nu}_{i+\frac{1}{2},j-\frac{1}{2}}\right), \tag{55}$$

where we recall that $(\delta y u)^{*}_{i+\frac{1}{2},j}$ are the preliminary quantities obtained from the explicit discretization of the convective terms. To complete the FV scheme, classical *two*-point fluxes based on the mid-point rule are chosen and they are defined in the x- and y-directions as

$$f^{\nu}_{i+1,j} = \nu\delta y^n_{i+1,j}\frac{u^n_{i+\frac{3}{2},j} - u^n_{i+\frac{1}{2},j}}{\Delta x} \tag{56}$$

and

$$g^{\nu}_{i+\frac{1}{2},j+\frac{1}{2}} = \nu\delta y^n_{i+\frac{1}{2},j+\frac{1}{2}}\frac{u^n_{i+\frac{1}{2},j+1} - u^n_{i+\frac{1}{2},j}}{\Delta y} \tag{57}$$

with $\delta y^n_{i+1,j} = \frac{1}{2}(\delta y^n_{i+1/2,j} + \delta y^n_{i+3/2,j})$, $\delta y^n_{i+\frac{1}{2},j+\frac{1}{2}} = \frac{1}{2}(\delta y^n_{i+1/2,j+1} + \delta y^n_{i+1/2,j})$. The same can be done in the y-direction. The discretization of the gravity contribution, included in the source term, is explicitly added to these intermediate states $(\delta y u)^{**}_{i+\frac{1}{2},j}$, $(\delta x v)^{**}_{i,j+\frac{1}{2}}$.

Implicit discretization of the pressure subsystem and source term The contribution of the pressure to the momentum equation has to be discretized implicitly. The two equations, in the x- and y-directions read, respectively,

$$\frac{\partial \alpha^l u}{\partial t} + \alpha^l\frac{\partial p}{\partial x} = 0 \quad \text{and} \quad \frac{\partial \alpha^l v}{\partial t} + \alpha^l\frac{\partial p}{\partial y} = 0, \tag{58}$$

and as for the previous viscous subsystem, the two equations have to be discretized over two different staggered edge-based control volumes in the x- and y-directions. In the x-direction, the PDE is integrated over the staggered edge-based cells $\Omega_{i+\frac{1}{2},j} \times [t^n, t^{n+1}]$, which is represented in Fig. 2, and reads

$$\int_{t^{**}}^{t^{n+1}} \int_{x_i}^{x_{i+1}} \int_{y_{j-\frac{1}{2}}}^{y_{j+\frac{1}{2}}} \frac{\partial \alpha^l u}{\partial t} \mathrm{d}x\mathrm{d}y\mathrm{d}t + \int_{t^{**}}^{t^{n+1}} \int_{x_i}^{x_{i+1}} \int_{y_{j-\frac{1}{2}}}^{y_{j+\frac{1}{2}}} \alpha^l \frac{\partial p}{\partial x} \mathrm{d}x\mathrm{d}y\mathrm{d}t = 0. \tag{59}$$

Assuming that the discrete pressure is piecewise constant in each cell

$$p(x) = \begin{cases} p_{i,j}, & \text{if } x \leqslant x_{i+\frac{1}{2}}, \\ p_{i+1,j}, & \text{if } x > x_{i+\frac{1}{2}}, \end{cases} \tag{60}$$

then

$$\frac{\partial p}{\partial x} = \delta(x - x_{i+\frac{1}{2}})\big(p_{i+1} - p_i\big),$$

and integrating in the x-direction, the non-conservative product reads

$$\Delta x \Delta y \left((\alpha^l u)^{n+1}_{i+\frac{1}{2},j} - (\alpha^l u)^{**}_{i+\frac{1}{2},j} \right) + \int_{t^{**}}^{t^{n+1}} \int_{y_{j-\frac{1}{2}}}^{y_{j+\frac{1}{2}}} \tilde{\alpha}_{i+\frac{1}{2},j}\big(p_{i+1,j} - p_{i,j}\big) \mathrm{d}y\mathrm{d}t = 0, \tag{61}$$

where $\tilde{\alpha}_{i+\frac{1}{2},j}$ is defined with the path integral along the straight-line segment path $\varphi = \alpha_i + s(\alpha_{i+1} - \alpha_i)$ and results $\tilde{\alpha}_{i+\frac{1}{2},j} = \frac{1}{2}(\alpha_{i+1,j} + \alpha_{i,j})$. Then introducing this definition in (61) and integrating, the following implicit discretization of the pressure terms is obtained:

$$\Delta x \Delta y \left((\alpha^l u)^{n+1}_{i+\frac{1}{2},j} - (\alpha^l u)^{**}_{i+\frac{1}{2},j} \right) + \Delta t \Delta y \delta y_{i+\frac{1}{2},j} \left(p^{n+1}_{i+1,j} - p^{n+1}_{i,j} \right) = 0, \tag{62}$$

where $\delta y_{i+\frac{1}{2},j} = \Delta y \tilde{\alpha}_{i+\frac{1}{2},j} = \Delta y \frac{1}{2}({\alpha^l}_{i+1,j} + {\alpha^l}_{i,j})$. The two discrete momentum equations, in the x- and y-directions, including the discretization of the non-conservative pressure terms therefore read

$$(\delta y u)^{n+1}_{i+\frac{1}{2},j} = (\delta y u)^{**}_{i+\frac{1}{2},j} - \Delta t \, \delta y^{n+1}_{i+\frac{1}{2},j} \frac{p^{n+1}_{i+1,j} - p^{n+1}_{i,j}}{\Delta x} \tag{63}$$

and

$$(\delta x v)^{n+1}_{i,j+\frac{1}{2}} = (\delta x v)^{**}_{i,j+\frac{1}{2}} - \Delta t \, \delta x^{n+1}_{i,j+\frac{1}{2}} \frac{p^{n+1}_{i,j+1} - p^{n+1}_{i,j}}{\Delta y}. \tag{64}$$

The algebraic velocity relaxation source term contained in $\mathbf{S}(\mathbf{Q})$ still needs to be discretized. It requires an implicit discretization on the same staggered control volumes, where a simple backward Euler scheme is used. By adding this contribution to (64), the final semi-implicit discretization of the momentum equations is obtained as

$$\begin{cases} (\delta yu)^{n+1}_{i+\frac{1}{2},j} = (\delta yu)^{**}_{i+\frac{1}{2},j} - \dfrac{\Delta t}{\Delta x}\delta y^{n+1}_{i+\frac{1}{2},j}\,(p^{n+1}_{i+1,j} - p^{n+1}_{i,j}) \\ \qquad\qquad - \dfrac{\Delta t}{\epsilon}\,\delta y^{n+1}_{i+\frac{1}{2},j}\,(u^{n+1}_{i+\frac{1}{2},j} - u^{s,n+1}_{i+\frac{1}{2},j})\alpha^{s,n+1}_{i+\frac{1}{2},j}, \\ (\delta xv)^{n+1}_{i,j+\frac{1}{2}} = (\delta xv)^{**}_{i,j+\frac{1}{2}} - \dfrac{\Delta t}{\Delta y}\delta x^{n+1}_{i,j+\frac{1}{2}}\,(p^{n+1}_{i,j+1} - p^{n+1}_{i,j}) \\ \qquad\qquad - \dfrac{\Delta t}{\epsilon}\,\delta x^{n+1}_{i,j+\frac{1}{2}}\,(v^{n+1}_{i,j+\frac{1}{2}} - v^{s,n+1}_{i,j+\frac{1}{2}})\alpha^{s,n+1}_{i,j+\frac{1}{2}}, \end{cases} \tag{65}$$

where $\alpha^{s,n+1}_{i+\frac{1}{2},j}$ and $\alpha^{s,n+1}_{i,j+\frac{1}{2}}$ are referring to the edge, then they can be evaluated either as the maximum or the average of the ones in the adjacent cells.

Manipulating the previous equations, $(\delta yu)^{n+1}_{i+\frac{1}{2},j}$ and $(\delta xv)^{n+1}_{i,j+\frac{1}{2}}$ can be expressed as follows:

$$\begin{aligned} (\delta yu)^{n+1}_{i+\frac{1}{2},j}\left(1 + \frac{\Delta t}{\epsilon}\,\alpha^{s,n+1}_{i+\frac{1}{2},j}\right) &= (\delta yu)^{**}_{i+\frac{1}{2},j} - \frac{\Delta t}{\Delta x}\delta y^{n+1}_{i+\frac{1}{2},j}\,(p^{n+1}_{i+1,j} - p^{n+1}_{i,j}) \\ &\quad + \frac{\Delta t}{\epsilon}\,\delta y^{n+1}_{i+\frac{1}{2},j}\,u^{s,n+1}_{i+\frac{1}{2},j}\alpha^{s,n+1}_{i+\frac{1}{2},j}, \end{aligned} \tag{66}$$

$$\begin{aligned} (\delta xv)^{n+1}_{i,j+\frac{1}{2}}\left(1 + \frac{\Delta t}{\epsilon}\,\alpha^{s,n+1}_{i,j+\frac{1}{2}}\right) &= (\delta xv)^{**}_{i,j+\frac{1}{2}} - \frac{\Delta t}{\Delta y}\delta x^{n+1}_{i,j+\frac{1}{2}}\,(p^{n+1}_{i,j+1} - p^{n+1}_{i,j}) \\ &\quad + \frac{\Delta t}{\epsilon}\,\delta x^{n+1}_{i,j+\frac{1}{2}}\,v^{s,n+1}_{i,j+\frac{1}{2}}\alpha^{s,n+1}_{i,j+\frac{1}{2}}, \end{aligned} \tag{67}$$

which can be rewritten as

$$\begin{aligned} (\delta yu)^{n+1}_{i+\frac{1}{2},j} =& \frac{\epsilon}{\alpha^{s,n+1}_{i+\frac{1}{2},j}\Delta t + \epsilon}\left((\delta yu)^{**}_{i+\frac{1}{2},j} - \frac{\Delta t}{\Delta x}\delta y^{n+1}_{i+\frac{1}{2},j}\,(p^{n+1}_{i+1,j} - p^{n+1}_{i,j})\right) \\ &+ \frac{\alpha^{s,n+1}_{i+\frac{1}{2},j}\Delta t}{\alpha^{s,n+1}_{i+\frac{1}{2},j}\Delta t + \epsilon}\,\delta y^{n+1}_{i+\frac{1}{2},j}\,u^{s,n+1}_{i+\frac{1}{2},j}, \end{aligned} \tag{68}$$

$$\begin{aligned} (\delta xv)^{n+1}_{i,j+\frac{1}{2}} =& \frac{\epsilon}{\alpha^{s,n+1}_{i,j+\frac{1}{2}}\Delta t + \epsilon}\left((\delta xv)^{**}_{i,j+\frac{1}{2}} - \frac{\Delta t}{\Delta y}\delta x^{n+1}_{i,j+\frac{1}{2}}\,(p^{n+1}_{i,j+1} - p^{n+1}_{i,j})\right) \\ &+ \frac{\alpha^{s,n+1}_{i,j+\frac{1}{2}}\Delta t}{\alpha^{s,n+1}_{i,j+\frac{1}{2}}\Delta t + \epsilon}\,\delta x^{n+1}_{i,j+\frac{1}{2}}\,v^{s,n+1}_{i,j+\frac{1}{2}}. \end{aligned} \tag{69}$$

Two different types of coefficients can be identified, for both equations, as $\beta^{n+1}_{i+\frac{1}{2},j}$, $\gamma^{n+1}_{i+\frac{1}{2},j}$ and $\beta^{n+1}_{i,j+\frac{1}{2}}$, $\gamma^{n+1}_{i,j+\frac{1}{2}}$; they read

$$\beta^{n+1}_{i+\frac{1}{2},j} = \frac{\epsilon}{\alpha^{s,n+1}_{i+\frac{1}{2},j}\Delta t + \epsilon}, \quad \gamma^{n+1}_{i+\frac{1}{2},j} = \frac{\alpha^{s,n+1}_{i+\frac{1}{2},j}\Delta t}{\alpha^{s,n+1}_{i+\frac{1}{2},j}\Delta t + \epsilon},$$
$$\beta^{n+1}_{i,j+\frac{1}{2}} = \frac{\epsilon}{\alpha^{s,n+1}_{i,j+\frac{1}{2}}\Delta t + \epsilon}, \quad \gamma^{n+1}_{i,j+\frac{1}{2}} = \frac{\alpha^{s,n+1}_{i,j+\frac{1}{2}}\Delta t}{\alpha^{s,n+1}_{i,j+\frac{1}{2}}\Delta t + \epsilon}.$$

Note the behavior of these coefficients as ϵ approaches to 0, assuming $\alpha^s = 1$, i.e., inside the solid phase, or assuming $\alpha^s = 0$ in the liquid phase:

$$\begin{cases} \lim\limits_{\epsilon\to 0} \beta^{n+1}_{i+\frac{1}{2},j}\Big|_{\alpha^s=1} = 0, & \lim\limits_{\epsilon\to 0} \gamma^{n+1}_{i+\frac{1}{2},j}\Big|_{\alpha^s=1} = 1, \\ \lim\limits_{\epsilon\to 0} \beta^{n+1}_{i+\frac{1}{2},j}\Big|_{\alpha^s=0} = 1, & \lim\limits_{\epsilon\to 0} \gamma^{n+1}_{i+\frac{1}{2},j}\Big|_{\alpha^s=0} = 0. \end{cases} \tag{70}$$

Thus, when a cell is completely occupied by the solid phase, the momentum equations automatically and naturally force the velocity of the residual liquid phase to tend to the velocity of the solid phase.

3.4 Final Pressure System

Inserting the discrete momentum equations (69) into the FV discretization of the continuity equation (32) yields the following system for the unknown pressure $p^{n+1}_{i,j}$:

$$\begin{aligned} &V(p^{n+1}_{i,j}) - \frac{\Delta t^2}{\Delta x}\left(\beta^{n+1}_{i+\frac{1}{2},j}\delta y^{n+1}_{i+\frac{1}{2},j}(p^{n+1}_{i+1,j} - p^{n+1}_{i,j}) - \beta^{n+1}_{i-\frac{1}{2},j}\delta y^{n+1}_{i-\frac{1}{2},j}(p^{n+1}_{i,j} - p^{n+1}_{i-1,j})\right) \\ &- \frac{\Delta t^2}{\Delta y}\left(\beta^{n+1}_{i,j+\frac{1}{2}}\delta x^{n+1}_{i,j+\frac{1}{2}}(p^{n+1}_{i,j+1} - p^{n+1}_{i,j}) - \beta^{n+1}_{i,j-\frac{1}{2}}\delta x^{n+1}_{i,j-\frac{1}{2}}(p^{n+1}_{i,j} - p^{n+1}_{i,j-1})\right) = b^n_{i,j} \end{aligned} \tag{71}$$

with the known right-hand side $b^n_{i,j}$

$$\begin{aligned} b^n_{i,j} = V(p^n_{i,j}) &- \Delta t\left(\gamma^{n+1}_{i+\frac{1}{2},j}(\delta yu)^{s,n+1}_{i+\frac{1}{2},j} - \gamma^{n+1}_{i-\frac{1}{2},j}(\delta yu)^{s,n+1}_{i-\frac{1}{2},j}\right) \\ &- \Delta t\left(\gamma^{n+1}_{i,j+\frac{1}{2}}(\delta xv)^{s,n+1}_{i,j+\frac{1}{2}} - \gamma^{n+1}_{i,j-\frac{1}{2}}(\delta xv)^{s,n+1}_{i,i-\frac{1}{2}}\right) \\ &- \Delta t\left(\beta^{n+1}_{i+\frac{1}{2},j}(\delta yu)^{*}_{i+\frac{1}{2},j} - \beta^{n+1}_{i-\frac{1}{2},j}(\delta yu)^{**}_{i-\frac{1}{2},j}\right) \\ &- \Delta t\left(\beta^{n+1}_{i,j+\frac{1}{2}}(\delta xv)^{*}_{i,j+\frac{1}{2}} - \beta^{n+1}_{i,j-\frac{1}{2}}(\delta xv)^{**}_{i,j-\frac{1}{2}}\right). \end{aligned} \tag{72}$$

Discretizing the edge-integrated volume fractions $\delta x^{n+1}_{i,j+\frac{1}{2}}$, $\delta y^{n+1}_{i+\frac{1}{2},j}$ and the velocities of the objects $u^{s,n+1}$, $v^{s,n+1}$ implicitly, the system (71) becomes strongly nonlinear and thus difficult to solve. Actually, the solid related variables $u^{s,n+1}$, $v^{s,n+1}$, and $\alpha^{s,n+1}$ are known at time

t^{n+1} due to the fact that the kinematics of the solid is decoupled from the dynamics of the liquid phase, thus the non-linearity affects only the edge-integrated volume fractions. Therefore, a *Picard iteration* technique has to be adopted to make the edge-integrated volume fractions $\delta x^{n+1}_{i,j+\frac{1}{2}}$, $\delta y^{n+1}_{i+\frac{1}{2},j}$ explicit again, as suggested in [20].

Introducing k to denote the index of the Picard iterations, the following *mildly non-linear* system for the pressure $p^{n+1,k+1}_{i,j}$ is obtained:

$$\begin{aligned} V(p^{n+1,k+1}_{i,j}) &- \frac{\Delta t^2}{\Delta x}\left(\beta^{n+1}_{i+\frac{1}{2},j}\,\delta y^{n+1,k}_{i+\frac{1}{2},j}\,\Delta p^{n+1,k+1}_{i+\frac{1}{2},j} - \beta^{n+1}_{i-\frac{1}{2},j}\,\delta y^{n+1,k}_{i-\frac{1}{2},j}\,\Delta p^{n+1,k+1}_{i-\frac{1}{2},j}\right) \\ &- \frac{\Delta t^2}{\Delta y}\left(\beta^{n+1}_{i,j+\frac{1}{2}}\,\delta x^{n+1,k}_{i,j+\frac{1}{2}}\,\Delta p^{n+1,k+1}_{i,j+\frac{1}{2}} - \beta^{n+1}_{i,j-\frac{1}{2}}\,\delta x^{n+1,k}_{i,j-\frac{1}{2}}\,\Delta p^{n+1,k+1}_{i,j-\frac{1}{2}}\right) = b^n_{i,j} \end{aligned} \tag{73}$$

with $\Delta p^{n+1,k+1}_{i+\frac{1}{2},j} = p^{n+1,k+1}_{i+1,j} - p^{n+1,k+1}_{i,j}$ and $\Delta p^{n+1,k+1}_{i,j+\frac{1}{2}} = p^{n+1,k+1}_{i,j+1} - p^{n+1,k+1}_{i,j}$. The system (73) needs to be solved for the pressure $p^{n+1,k+1}_{i,j}$ at each Picard iteration. Using a more compact notation, the above system can be written as follows:

$$\boldsymbol{V}(\boldsymbol{p}^{n+1,k+1}) + \boldsymbol{T}\boldsymbol{p}^{n+1,k+1} = \boldsymbol{b}^n \tag{74}$$

with the vector of the unknown new pressure $\boldsymbol{p}^{n+1,k+1} = (p^{n+1,k+1}_{i,j})$ and where $\boldsymbol{V}(\boldsymbol{p}^{n+1,k+1}) = \left(V(p^{n+1,k+1}_{i,j})\right)$ denotes the corresponding fluid volumes; $\boldsymbol{b}^n$ is the known right-hand side vector and $\boldsymbol{T}$ is a sparse, symmetric, and penta-diagonal matrix which arises from the linear terms in (73). The matrix $\boldsymbol{T}$ in the system (74) is symmetric and at least positive semi-definite. For the solution of system (74), we apply the nested Newton-type technique introduced by Brugnano et al. [9, 10, 20, 21], associated with a matrix-free implementation of the conjugate gradient method. For implementation details and the convergence proofs of these Newton-type techniques applied to mildly nonlinear systems the reader is referred to the above references.

Once the pressures $p^{n+1,k+1}_{i,j}$ are evaluated, the quantities $\delta y^{n+1,k}_{i+\frac{1}{2},j}$ and $\delta x^{n+1,k}_{i,j+\frac{1}{2}}$ at the next Picard iteration can be easily obtained from (33) and (34). As confirmed by numerical simulations, only very few Picard iterations are needed to obtain an accurate solution. At the end of the last Picard iteration $p^{n+1}_{i,j} := p^{n+1,k+1}_{i,j}$ is set and the velocity field is easily obtained from the discrete momentum equations (69). The time step is only limited by a *mild* CFL condition based on the liquid and solid phase velocities and the kinematic viscosity. Since the solid phase is also governed by an advection equation which is explicitly discretized and since the velocity of the solid phase is prescribed *a priori*, a stability condition that is valid for both phases can be easily formulated. For the explicit advection terms of both phases and all the test problems shown in this paper the CFL time restriction reads

$$\Delta t \leqslant \frac{\mathrm{CFL}}{\frac{s^{\max}_x}{\Delta x} + \frac{2\nu}{\Delta x^2} + \frac{s^{\max}_y}{\Delta y} + \frac{2\nu}{\Delta y^2}}, \tag{75}$$

where the choice of the maximum wave speed is $s^{\max}_x = 2\max(|u|, |u^s|)$ and $s^{\max}_y = 2\max(|v|, |v^s|)$ and ν is the kinematic viscosity coefficient. The stability condition is not affected by the gravity wave speed, thus the method is efficient for low Froude number flows, too.

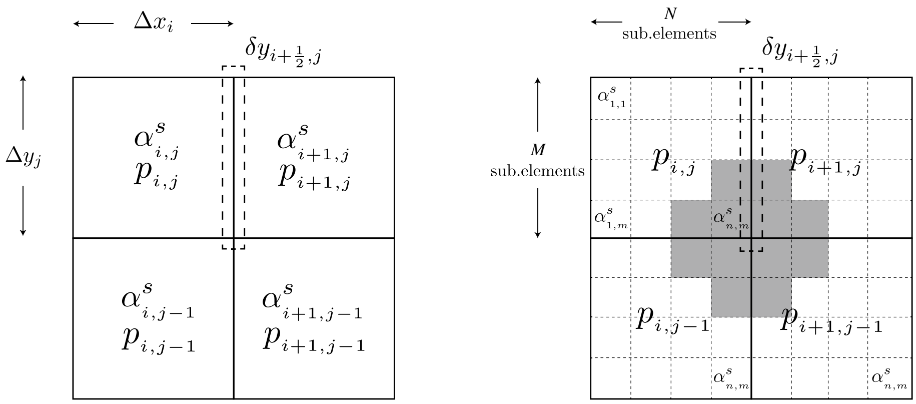

Fig. 3 Representation of the main grid for the evaluation of the liquid phase related variables (left). Representation of the sub-grid within the main grid for the evaluation of the refined solid phase variables (right). In gray is depicted the variability of the solid volume fraction $\alpha^s_{n,m}$ over the sub-grid

3.5 Advection of the Solid Volume Fraction Using a Subgrid

The solid phase kinematics is prescribed and is evaluated through an advection equation, as described in (1). However, it is necessary for the advection of the solid phase to be accurately computed to preserve the properties of a solid, i.e., to remain sharply defined and to spread only slightly over time due to the numerical viscosity of the scheme. Usually, a numerical method is able to produce better solutions as the mesh size is refined. However, the adoption of a too severe grid refinement, to ensure an accurate advection of the solid phase, can easily become computationally prohibitive for the evaluation of the liquid phase dynamics, which requires the solution of an implicit pressure equation. A practical solution, which is adopted in all the test problems shown in this paper, is to keep the main computational grid at a reasonable size and adopt a sub-grid strategy to evaluate the advection of the solid volume fraction α^s and the effective edge-integrated volume fractions $\delta y^{n+1}_{i+\frac{1}{2},j}$ and $\delta x^{n+1}_{i,j+\frac{1}{2}}$, similar to the subgrid methods introduced in other contexts in [19, 28].

As represented in Fig. 3, starting from the main grid, which consists of rectangular control volumes $\Omega_{i,j} = [x_{i-\frac{1}{2}}, x_{i+\frac{1}{2}}] \times [y_{j-\frac{1}{2}}, y_{j+\frac{1}{2}}]$ with barycenters in (x_i, y_j) and having width Δx_i and height Δy_j, a sub-grid consisting of $N \times M$ sub-elements for each rectangular control volumes $\Omega_{i,j}$ is defined.

The cell-averaged solid volume fraction α^s is defined on this sub-grid as follows:

$$\alpha^s_{n,m} = \frac{NM}{\Delta x \Delta y} \int_{x_{n-\frac{1}{2}}}^{x_{n+\frac{1}{2}}} \int_{y_{m-\frac{1}{2}}}^{y_{m+\frac{1}{2}}} \alpha^s(x,y)\mathrm{d}y\mathrm{d}x, \tag{76}$$

while on the main grid, a cell-averaged solid volume fraction $\alpha^s_{i,j}$ can be evaluated by means of the values in these subcells

$$\alpha^s_{i,j} = \frac{1}{NM} \sum_{n,m=1}^{N,M} \alpha^s_{n,m}. \tag{77}$$

Furthermore, the edge-integrated effective volume fractions can be more accurately assessed, in agreement with the more accurate distribution of the solid phase on the sub-grid. Considering for instance the edge-integrated effective volume fraction $\delta y^{n+1}_{i+\frac{1}{2},j}$ shown in Fig. 3, it can be evaluated over the sub-grid as follows:

$$\delta y_{i+\frac{1}{2},j} = \frac{N}{2\Delta x} \sum_{m=1}^{M} \Big(V^l(p_{i,j}, \alpha^s_{n,m}) + V^l(p_{i+1,j}, \alpha^s_{1,m}) \Big), \tag{78}$$

where the liquid cell volume V^l is evaluated by the constitutive relationship scaled for the sub-grid and the sub-grid cell-averages of the solid volume fraction $\alpha^s_{n,m}$ which shares the same edge are involved.

Moreover, a higher order method to evaluate the advection of the solid phase can be used, in particular again in this paper the second order in space and time is achieved with the aid of a MUSCL-Hancock TVD method, see [56] for details.

4 Numerical Results

In this section, the numerical scheme presented previously is validated on a set of different classical test problems for the incompressible Navier-Stokes equations for which an analytical or numerical reference solution exists. It is interesting to note that, most of the tests are formulated in such a way that two phases, the solid and liquid phases, are always present. This is to test the ability of the method to automatically solve two-phase flows, i.e., two phases are simulated quite often to assess that the boundary conditions between phases are automatically well imposed by solving the PDE.

In all the tests, the time step Δt is computed according to the CFL condition expressed in (75), based on the liquid and solid velocities and the kinematic viscosity, assuming a CFL number set to 0.9. Moreover, the gravity is assumed to be constant and equal to $g = 9.81$ and it is recalled that p was defined, in Sect. 2, as the normalized pressure, i.e., the pressure divided by the density, which is assumed to be constant and equal to $\rho = 1\,000$. Finally, after conducting various numerical tests, it was found that it is enough to assume the scale for the velocity relaxation kinetics is equal to $\epsilon = 10^{-4}$. Throughout this section, unless explicitly noted, we adopt SI units for all quantities.

4.1 The First Problem of Stokes

The first problem of Stokes [46] is one of the few test problems for which an exact analytical solution of the unsteady Navier-Stokes equations is known. This problem consists of the time-evolution of an infinite incompressible shear layer. The computational domain is $\Omega = [-0.5; 0.5] \times [-0.5; 0.5]$ with velocity imposed on the left and right boundaries and periodic boundary conditions along the y-direction. The initial conditions of the problem are given by

$$\alpha^l(x,y,0) = 1, \quad \alpha^s(x,y,0) = 0, \quad p(x,y,0) = \beta,$$
$$v^l(x,y,0) = 0, \quad u^l(x,y,0) = \begin{cases} 0.1, & \text{if } x > 0, \\ -0.1, & \text{if } x \leqslant 0, \end{cases}$$

where $\beta = g\frac{\Delta y}{2}$ as defined in Sect. 3.1. Simulations are performed assuming two different kinematic viscosities $\nu = 10^{-2}$ and $\nu = 10^{-4}$.

The exact analytical solution of the incompressible Navier-Stokes equations for the velocity component u is given by the following error function:

$$u(x,t) = u_0 \mathrm{erf}\left(\frac{1}{2}\frac{x}{\sqrt{\nu t}}\right). \tag{79}$$

The computational domain is covered by a uniform rectangular grid consisting of 100×100 elements with the mesh spacings $\Delta x, \Delta y = 0.01$ in both x- and y-directions.

The comparison between the computational results along the line $y = 0$, up to the final time $t = 1.0$, and the exact solution of the first problem of Stokes for the Navier-Stokes equations are depicted in Fig. 4. Even with a quite coarse mesh the numerical solution is in good agreement with the exact solution, also by varying the kinematic viscosity.

4.2 Two-Dimensional Taylor-Green Vortex

The Taylor-Green vortex is another test problem for which an exact solution of the incompressible Navier-Stokes equations with periodic boundary conditions can be found. This test is widely used for testing the accuracy of numerical schemes, because it has a smooth unsteady analytical solution, which is a two-dimensional decaying vortex. In other words, the initial sinusoidal velocity field is smoothed over time by the viscous stresses. In a two-dimensional space, the analytical solution reads

$$\begin{cases} u(x,y,t) = \sin(x)\cos(y)\mathrm{e}^{-2\nu t}, \\ v(x,y,t) = -\cos(x)\sin(y)\mathrm{e}^{-2\nu t}, \\ p(x,y,t) = 1/4(\cos(2x) + \cos(2y))\mathrm{e}^{-4\nu t}. \end{cases} \tag{80}$$

The computational domain is $\Omega = [0; 2\pi]^2$ with periodic boundary conditions on all the boundaries. To conduct a convergence study, the initial condition of the problem is given by the exact solution (80), assuming $t = 0$, and the kinematic viscosity is assumed to be $\nu = 10^{-1}$. The standard way to get the numerical order of accuracy is to refine the mesh spacing and to look at the ratio of the obtained numerical errors. Four simulations are carried out and in Table 1 the meshes used are listed. For these tests a final time $t_{\mathrm{end}} = 0.1$ is considered and the time step Δt is determined following the CFL condition.

The computational results, for the coarsest mesh M_1, are depicted in Fig. 5, where the pressure contour and the velocity field are represented. A comparison of the two velocity components with the exact solution of the incompressible Navier-Stokes equations is shown on the right. A simple qualitative observation shows excellent agreement between the numerical solution and the reference solution for both velocity components. The L_1 and L_2 norms of the error and the corresponding convergence rates are presented in Table 1 for the variable u, and are defined as follows:

$$E(u) = ||u - u_{M_i}||_{(L^p(\Omega))}, \quad o(u_{M_i/M_j}) = \log\left(\frac{E(u)_{M_i}}{E(u)_{M_j}}\right) \Big/ \log\left(\frac{h_{M_i}}{h_{M_j}}\right), \tag{81}$$

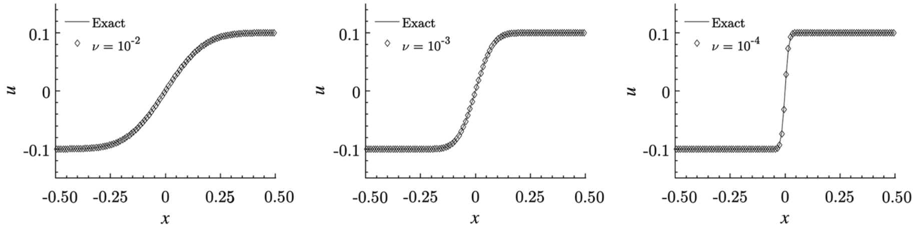

Fig. 4 Exact (solid line) and numerical solutions of the first problem of Stokes for the Navier-Stokes equations for the velocity component u at time = 1. Different viscosities are simulated, from left to right, $\nu = 10^{-2}$ and $\nu = 10^{-4}$

where p denotes the order of the norm.

In Fig. 6 these two norms are represented graphically against the number of elements of the mesh with respect to the optimal second-order convergence. The calculated convergence rates, corresponding to the two norms, are also shown in Table 1, and, as expected, the numerical scheme, here presented, essentially achieves the second order of accuracy.

4.3 Blasius Boundary Layer

The boundary layer equations of Prandtl [43] were solved for the first time in the particular case of a steady laminar boundary layer over a flat plate by Blasius [5]. For an overview of the boundary layer theory, see [46]. Blasius proposed a similarity solution that reduces the boundary layer equations to the solution of a third order non-linear ordinary differential equation (ODE), which reads

$$f''' + ff'' = 0, \tag{82}$$

where the prime denotes the derivation with respect to η, which is the introduced self-similar variable $\eta = y\sqrt{\frac{U}{2\nu x}}$. Then the boundary conditions which have to be imposed are the no-slip condition, the impermeability of the wall, and the free stream velocity outside the boundary layer, $u(x,0) = 0$, $v(x,0) = 0$, and $u(x,\infty) = U$, where U is the free stream velocity and it is a constant. This ODE can be easily solved numerically, e.g., the reference solution in this paper is computed by a Runge-Kutta scheme of order four in combination with a classical shooting technique.

The computational domain is $\Omega = [-0.004; 0.1] \times [-0.5; 0.5]$, hence, it includes the solid wall, and is discretized with $2\,000 \times 208$ rectangular elements. The initial conditions of the problem for each phase, are given by

$$\begin{cases} \alpha^l(x,y,0) = \begin{cases} 1, & \text{if } x > 0, \\ 1\mathrm{e}^{-14}, & \text{if } x \leqslant 0, \end{cases} & \\ \alpha^s(x,y,0) = \begin{cases} 1\mathrm{e}^{-14}, & \text{if } x > 0, \\ 1, & \text{if } x \leqslant 0, \end{cases} & p(x,y,0) = p_{\text{out}}, \\ u_i^s(x,y,0) = 0, \quad v(x,y,0) = 0, \quad u(x,y,0) = 1. & \end{cases} \tag{83}$$

The kinematic viscosity is assumed to be very low $\nu = 10^{-5}$, which leads to a very thin boundary layer and then the Reynolds number of the flow is $Re = 10^5$. At the right and

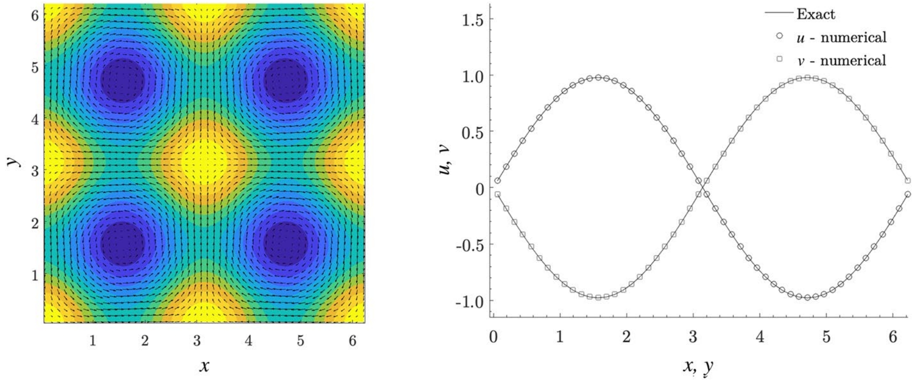

Fig. 5 Numerical solution for the Taylor-Green vortex at the final time $t = 0.1$, for the coarsest mesh M_1 and with a viscosity of $\nu = 10^{-1}$ (left). One-dimensional comparison of the velocity components u, v, with the exact solution of the incompressible Navier-Stokes equations along the x and y axes (right)

top outlet boundary conditions are set by imposing a constant pressure $p_{\text{out}} = 50\beta$ while at $x = 0$ the inflow boundary condition is given by the initial conditions.

It is important to note that it is not necessary to impose the no-slip boundary conditions along the flat plate, i.e., along the solid phase; the relaxation source term and the numerical method automatically impose these boundary conditions between the two phases in the correct way by solving the PDE. As the shape of the solid phase becomes more complex, this feature of the method will be of primary importance. In Fig. 7 (left), the computational results obtained for the horizontal velocity field u, computed at time $t = 10$, are shown, together with a velocity profile at $x = 0.1$. A comparison of this numerical velocity profile against the Blasius reference solution is made in Fig. 7 (right). The solid phase, characterized by $u^s(x, y, t) = v^s(x, y, t) = 0$, is shown in Fig. 7 in dark blue. A very good agreement between these two solutions can be observed, despite the fact that the no-slip boundary conditions along the flat plate are not imposed explicitly but just via the presence of a solid volume fraction for $y < 0$ and the stiff velocity relaxation source terms are presented in the PDE. This confirms the validity of the proposed numerical method to compute boundary layers correctly and thus compute viscous incompressible two-phase flows in a correct way.

4.4 Planar Hagen-Poiseuille Flow

The Hagen-Poiseuille flow describes a steady-state velocity and pressure distribution for a viscous fluid in laminar flow between two plates whose length L is much greater than the constant distance d separating them. The flow is driven by a constant pressure gradient $-\Delta p$ prescribed by the boundary conditions, which is balanced by the viscous drag along

Table 1 Mesh name, mesh elements, L_1- and L_2-error norms and their respective numerical convergence rates, o_{L^1} and o_{L^2}, for the variable u, applied to the two-dimesional Taylor-Green vortex

Mesh	Elements	E_{L^1}	o_{L^1}	E_{L^2}	o_{L^2}
M_1	50×50	4.591 3E−02		8.842 0E−03	
M_2	100×100	1.250 8E−02	1.87	2.423 2E−03	1.87
M_3	200×200	3.340 5E−03	1.90	6.544 2E−04	1.89
M_4	400×400	8.851 4E−04	1.92	1.739 4E−04	1.91

Fig. 6 L_1- and L_2-norms error against reciprocal of the cell size. The dashed line shows the theoretical second-order for comparison

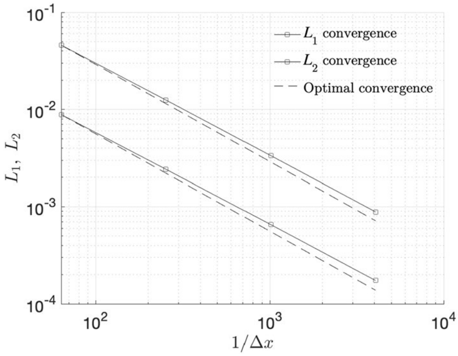

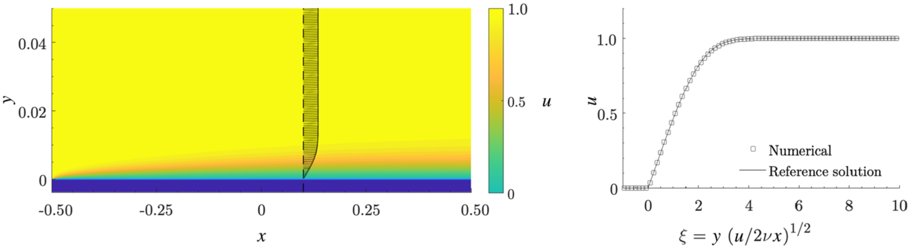

Fig. 7 Numerical solution for the laminar boundary layer over a flat solid plate (dark blue) with $Re = 10^5$ at the final time $t = 10.0$. The horizontal velocity u contours and a velocity profile in $x = 0.1$ are shown (left). Comparison of the numerical velocity profile at $x = 0.1$ against the Blasius reference solution (right)

both plates. This test, which satisfies the Hagen-Poiseuille flow, has a well known parabolic solution for the horizontal velocity profile u, given by

$$u = \frac{1}{2}\frac{\Delta p}{\nu L}\left(\frac{d^2}{4} - y^2\right). \tag{84}$$

This test is simulated on a domain $\Omega = [-2.5; 2.5] \times [-0.3; 0.3]$ which is discretized with $1\,000 \times 120$ rectangular elements, and the initial conditions for each phase are given by

$$\alpha^l(x,y,0) = \begin{cases} 1, & \text{if } |x| \leqslant 0.25, \\ 1\mathrm{e}^{-14}, & \text{if } |x| > 0.25, \end{cases}$$

$$\alpha^s(x,y,0) = \begin{cases} 1, & \text{if } |x| > 0.25, \\ 1\mathrm{e}^{-14}, & \text{if } |x| \leqslant 0.25, \end{cases}$$

$$p(-2.5,y,0) = 10\beta + 2.4, \quad p(2.5,y,0) = 10\beta, \quad u_i^s(x,y,0) = u_i(x,y,0) = 0.$$

The kinematic viscosity is assumed to be $\nu = 10^{-2}$. Therefore, the pressure gradient imposed between the left inflow and the right outlet is $\Delta p = 2.4$. These conditions, according to the Hagen-Poiseuille flow, result in a mean flow velocity of $\bar{u} = 1$ and a maximum flow velocity of $u_{\max} = 1.5$. At the left inflow and at the right outlet the boundary conditions are given by the initial conditions, whereas, again, it is not necessary to impose the no-slip boundary conditions along the flat plates, i.e., along the solid phase. The boundary conditions are implicitly imposed via the stiff velocity relaxation source terms.

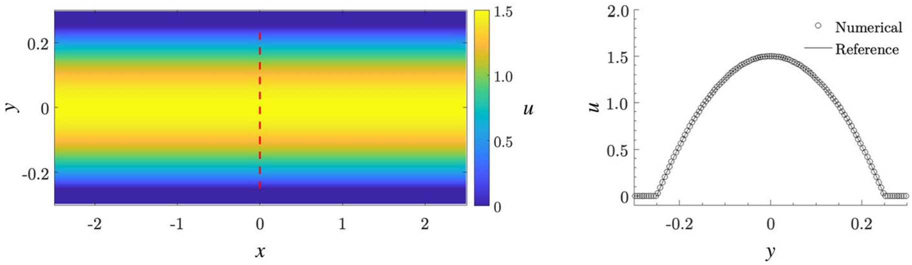

Fig. 8 Numerical solution for the laminar flow between two solid plates (dark blue) at a final time of $t = 50.0$. The horizontal velocity u contours is shown (left). Comparison of the numerical velocity profile at $x = 0$ against the reference solution of the Hagen-Poiseuille flow (right)

Left Fig. 8 shows the computational results obtained for the horizontal velocity field u, computed at time $t = 50$, while in the right one a comparison of this numerical velocity profile against the parabolic reference solution is made. The numerical solution is in good agreement with the reference solution of the Hagen-Poiseuille flow. The laminar flow is very well reproduced and the boundary conditions between the two phases are well resolved too.

4.5 Two-Dimensional Lid-Driven Cavity Problem

The lid-driven cavity is a fully two-dimensional classical reference problem for numerical methods applied to the incompressible Navier-Stokes equations, see [30, 36, 49]. In this test, a solid square cavity is considered, opened at the top and containing liquid which is driven by a lid imposed at the top.

This test is simulated on a domain $\Omega = [-0.55; 0.55] \times [-0.55; 0.5]$ which is discretized with 220×210 rectangular elements, and the initial conditions for each phase are given by

$$\alpha^l(x,y,0) = \begin{cases} 1\mathrm{e}^{-14}, & \text{if } |x| > 0.5 \text{ or } y < 0.5, \\ 1, & \text{otherwise}, \end{cases}$$

$$\alpha^s(x,y,0) = \begin{cases} 1, & \text{if } |x| > 0.5 \text{ or } y < 0.5, \\ 1\mathrm{e}^{-14}, & \text{otherwise}, \end{cases}$$

$$p(x,y,0) = 10\beta, \quad u_i^s(x,y,0) = 0, \quad u_i(x,y,0) = 0.$$

The kinematic viscosity is assumed to be $\nu = 10^{-2}$. The lid velocity is assumed to be equal to $u(x, 0.5, t) = 1$. Therefore, the Reynolds number of the flow is $Re = 100$. Also in this case it is not necessary to impose the no-slip boundary conditions along the solid phase square cavity explicitly, but they are automatically taken care of by the stiff velocity relaxation source term.

In Fig. 9, the computational results are shown and a comparison against the Navier-Stokes reference solution of Ghia et al. [36] is provided at time $t = 10$. In Fig. 9 (left) the velocity modulus contours are shown, while in dark blue the solid square cavity can be distinguished. It is important to emphasize that the description of the two phases has still been correctly resolved, automatically imposing the right boundary conditions. Again the numerical solution is in very good agreement with the reference solution.

4.6 Viscous Flow Over a Circular Cylinder

In this section, the viscous flow over a circular cylinder is considered for different Reynolds numbers. In previous work [34], an inviscid flow around the cylinder has been presented, to obtain a steady potential flow. Here, the viscous case is considered to observe the formation of the von Kármán vortex street.

The computational domain is taken sufficiently large $\Omega = [-3;15] \times [-10;10]$, to ensure that the boundary conditions affect the flow close to the cylinder the least. To obtain accurate results, unstructured meshes, see for instance in [49], are usually used to ensure a good representation of the geometry of the circular cylinder. However, in this work a simple uniform Cartesian grid is used and this leads to a particularly demanding test, since the geometry is only resolved via the diffuse interface approach. A rather large domain relative to the circular cylinder is required and at the same time a sufficiently refined grid is needed to represent the object correctly and to ensure that numerical viscosity is as low as possible. The domain is discretized with 720×800 rectangular elements. The initial conditions for each phase are given by

$$\alpha^l(x,y,0) = \begin{cases} 1\mathrm{e}^{-2}, & \text{if } \sqrt{x^2+y^2} \leqslant 1, \\ 1, & \text{otherwise,} \end{cases}$$

$$\alpha^s(x,y,0) = \begin{cases} 1 - 1\mathrm{e}^{-2}, & \text{if } \sqrt{x^2+y^2} \leqslant 1, \\ 0, & \text{otherwise,} \end{cases}$$

$$p(x,y,0) = p_{\mathrm{out}}, \quad u_i^s(x,y,0) = 0, \quad v(x,y,0) = 0, \quad u(x,y,0) = u_L,$$

where p_{out} is the pressure outside the domain while u_L is the inlet velocity, taken with the value 0.5. Different kinematic viscosity values are assumed to obtain simulations related to different Reynolds numbers, $Re = 75, 100, 125, 150$. At the upper, lower, and right boundaries, the outlet boundary conditions are set by imposing a constant pressure $p_{\mathrm{out}} = 50\beta$, while at the left boundary the velocity u_L is prescribed. It is not necessary to impose the no-slip boundary conditions along the solid phase circular cylinder.

As a first result, in Fig. 10 the von Kármán vortex street obtained at time $t = 300$ is shown for a $Re = 100$ flow. Here, to better visualize the typical structures of this viscous flow, the contour plot of a tracer added to the in-flow is shown. Moreover, to provide a qualitative

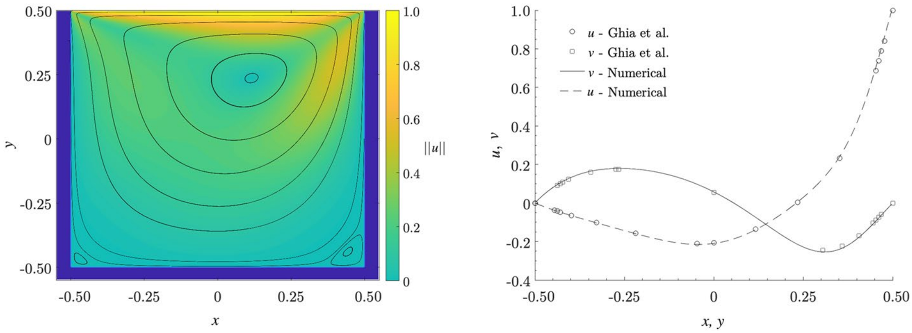

Fig. 9 Numerical solution for the lid driven cavity flow at time $t = 10$. The Reynolds number of the flow is $Re = 100$. The velocity module $\|u\|$ contour plot and streamlines are shown (left). Comparison of one-dimensional cuts of the velocity field against the Navier-Stokes reference solution of Ghia et al. [36] (right)

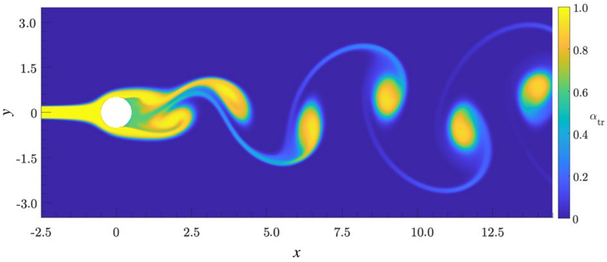

Fig. 10 Numerical solution for the laminar viscous flow past a circular cylinder at time $t = 300$, with $Re = 100$. The contour plot represents the concentration of the added tracer

comparison for this numerical test, the Strouhal number of the vortex shedding can be computed as

$$St = \frac{fL}{u}, \tag{85}$$

where f is the frequency of the oscillating flow mechanisms, L is the characteristic length of the cylinder, namely the diameter and u is the modulus of the flow velocity. The vortex-shedding frequency can be evaluated from the time series of the drag and lift coefficients. In fact, for a solid phase immersed in a viscous liquid phase, a net force can be evaluated from the pressure differences due to the flow. The lift component of this force is the one perpendicular to the incoming flow and the drag is the one parallel to the flow direction. From these two components the lift and drag coefficients can be evaluated, which read

$$C_l = \frac{2F_l}{\rho A u^2} \quad \text{and} \quad C_d = \frac{2F_d}{\rho A u^2}, \tag{86}$$

where F_d is the drag force, namely the resulting pressure force along the x-direction, and F_l the lift pressure force, A is the projected cylinder area, and u again is the velocity of the oncoming flow.

In Fig. 11 the lift and drag coefficients are represented for $Re = 100$. It is interesting to see how this numerical method is able to evaluate in a smooth way the pressure forces acting on the solid phase, and how the von Kármán vortex street develops over time to reach a periodic signal with a constant frequency and amplitude. This is the vortex-shedding frequency from which the Strouhal number of this oscillating signal can be computed. Carrying out several simulations with different Re, it is possible to recover the Strouhal-Reynolds number relationship.

Figure 12 shows a qualitative comparison between the numerical results obtained and some reference solutions, which are those obtained with the staggered space-time DG method [49] and the experimental data of Williamson and Brown [58].

It is possible to see that the Strouhal-Reynolds number relationship obtained with the numerical method presented in this paper is in agreement with experimental data and other numerical methods. However, a small discrepancy, which becomes more relevant as the Reynolds number increases, can be seen from the reference solutions. This is due to numerical viscosity, in fact achieving mesh convergence is computationally expensive for such a large domain using a uniform Cartesian grid.

4.7 Sloshing in a Moving Tank

In these last tests, some computational results are shown for incompressible two-phase flow problems, such as water flows interacting with moving solids and vacuum. In particular, this test considers the sloshing motion of a liquid phase in a partially filled solid tank, i.e., a free-surface flow problem in a moving solid geometry. The resulting flow is quite complex, characterized by the presence of high-amplitude oscillations and wave breaking, thus the non-hydrostatic effects cannot be neglected. Furthermore, to solve such a problem, a numerical method is required that is able to deal with the motion and interaction of two phases or with moving geometries. Actually, the most common method to solve this kind of problem is to use mobile geometries, i.e., to move the mesh according to the movement of the sloshing tank, as it has been done, for example, in [13, 25]. A thorough description of the testcase, as well as references to analytical studies and numerical results can be found in [13, 25] and references therein. Laboratory measurements of the wave height and hydrodynamic pressure have also been collected and reported such as those carried out by Faltinsen et al. [29].

As introduced earlier, to solve this problem through the numerical method presented in this paper, the dynamics of the liquid phase and the solid phase motion are decoupled. By solving the solid advection equation (1), with a prescribed solid velocity field u_k^s, one obtains the new solid volume fraction α^s distribution, which is needed in the constitutive relationship of the liquid phase volume (18) and in the relaxation source term. From the solution of (1) it is therefore possible to solve the system for the liquid phase (7).

The simulations presented in this paper refer to the numerical solutions obtained in [13, 25], which in turn refer to the tests presented in the work of Shao et al. [48], who presented an improved SPH method for the modeling liquid sloshing dynamics. The numerical methods presented in these papers, although different, include some kind of turbulence model to properly describe the effects of turbulence, since in the tests that will be addressed, the Reynolds number is of the order of $Re = 10^6$. However, in the semi-implicit FV scheme presented in this paper, a turbulence model has not been implemented, assuming that the eddy viscosity, as a rough approximation, is proportional to the numerical viscosity (ILES).

In this article, an idealized two-dimensional case is considered, where the tank, i.e., the solid phase, moves with a purely horizontal sinusoidal velocity and the vertical component of the velocity is zero, namely

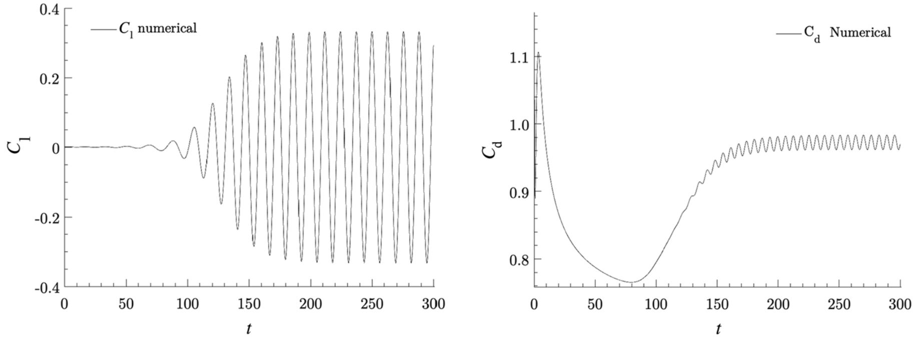

Fig. 11 The lift (left) and drag (right) coefficients for the solid circular cylinder immersed in a viscous flow. The Reynolds number of the flow is $Re = 100$

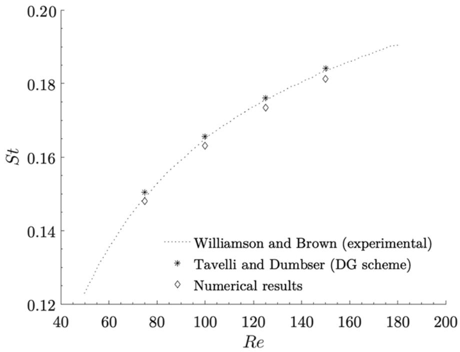

Fig. 12 Strouhal-Reynolds number relationship for the present numerical method compared with the experimental data of Williamson and Brown [58] and the numerical result of Tavelli and Dumbser [49]

$$u_s = \big(-\omega \delta x_A \sin(\omega t), 0\big), \tag{87}$$

where $\omega = \frac{2\pi}{T}$ is the frequency of the oscillation and T is the period, while δx_A represents the amplitude of the horizontal tank displacement which is assumed constant for all the tests and equal to $\delta x_A = 0.032$. The computational domain is taken large enough to include the experimental material and its displacements used for the laboratory measurements carried out by Faltinsen et al. [29], and large enough to describe the tank with a solid phase distribution, thus is taken equal to $\Omega = [-1 + \delta x_A;1 + \delta x_A] \times [-0.1;1.2]$. The initial conditions for each phase are given by

$$\alpha^l(x,y,0) = \begin{cases} 1, & \text{if } y \leqslant h_w, \\ 1\mathrm{e}^{-4}, & \text{otherwise,} \end{cases}$$

$$\alpha^s(x,y,0) = \begin{cases} 1 - 10^{-4}, & \text{if } |x - \delta x_A| \geqslant 0.865 \ \vee \ y < 0, \\ 0, & \text{otherwise,} \end{cases}$$

$$p(x,y,0) = \beta\left(\frac{2\,\alpha^l}{1-\alpha^s} - 1\right), \quad u_i^s(x,y,0) = 0, \quad u_i(x,y,0) = 0,$$

therefore, the fluid and the tank are set to be initially at rest and h_w is the initial free surface elevation. The domain is discretized with 720×800 rectangular elements. The kinematic viscosity is assumed to be $\nu = 10^{-6}$. Also in this test, the classical no-slip wall boundary conditions for the liquid phase, on the solid one, are automatically well imposed via the stiff velocity relaxation source terms.

Three simulations were carried out with three different parameter pairs, namely, the first pair of parameters $T = 1.3$ and $h_w = 0.6$, the second one $T = 1.5$ and $h_w = 0.6$, and the last pair $T = 1.875$ and $h_w = 0.5$. The sloshing dynamics, for the parameter pair $T = 1.5$ and $h_w = 0.6$, is depicted in Fig. 13 by nine instants representing a period of oscillation of the solid phase, namely the solid tank. Here, it is possible to see the presence of high-amplitude oscillations of the free surface occurring as the solid geometry moves, and the solid phase motion is also clearly detectable. Figure 14 shows a comparison, for the first pair of parameters $T = 1.3$ and $h_w = 0.6$, between the computed numerical solution, the experimental data provided by Faltinsen et al. [29] and the numerical results of Dumbser and Boscheri [25]. ΔH is the perturbation of the free surface elevation with respect to the initial at-rest condition. The numerical results were collected at the same probe point used in the two reference papers, which is fixed with respect to the solid phase, hence, it moves

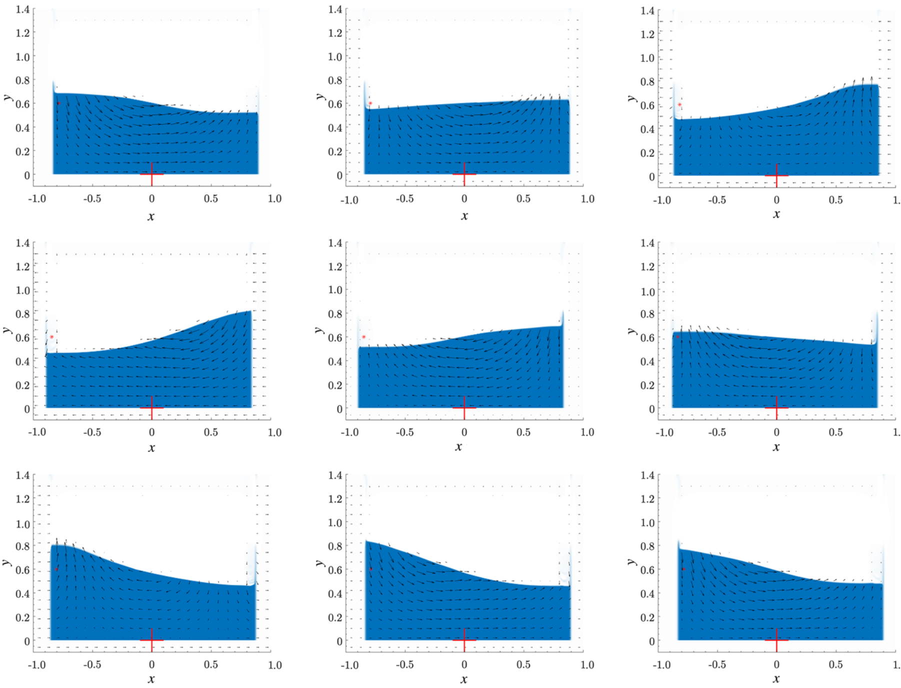

Fig. 13 The sloshing dynamics, for the parameter pairs $T = 1.5$ and $h_w = 0.6$, at times 3.0, 3.2, 3.4, 3.6, 3.8, 4.0, 4.2, 4.4, and 4.5 s

together with the tank. This point is located 0.05 m away from the left wall and ΔH is evaluated at each time step as

$$\Delta H = \left(\sum_j \alpha^l_{i_p,j} \mathrm{d}y \right) - h_w, \tag{88}$$

where i_p is the discrete index, in the x-direction, associated to the probe point which is moving horizontally according to the solid phase. It can be seen that the liquid phase reacts with a certain inertia to the movement of the solid phase. As the solid phase starts to move towards the left, the free surface on the left tends to decrease and then increase as the solid phase slows down to change direction around 1.2 s. The liquid phase keeps moving following the described periodic cycle of the solid phase with a free surface perturbation which is in overall good agreement with the experimental data and the numerically computed results of Dumbser and Boscheri [25].

Two more comparisons, for the second pair $T = 1.5$ and $h_w = 0.6$ and the last pair $T = 1.875$ and $h_w = 0.5$ of parameters, are depicted in Fig. 15. Here, it can be noticed how the amplitude of the wave progressively increases over time, due to a resonance effect. Again, results are in good agreement with the experimental data.

4.8 Water Entry of a Symmetric Wedge with Prescribed Velocity

In this last numerical simulation, a solid-fluid coupling problem is treated again in a free-surface flow context. In this test case a symmetric wedge impacting the free surface with

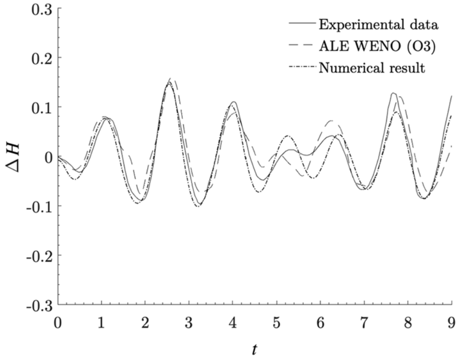

Fig. 14 Comparison for the sloshing in a moving tank test between the computed numerical solution, the experimental data provided by Faltinsen et al. [29] and the numerical results of Dumbser and Boscheri [25]. For the first pair of parameters $T = 1.3$ and $h_w = 0.6$

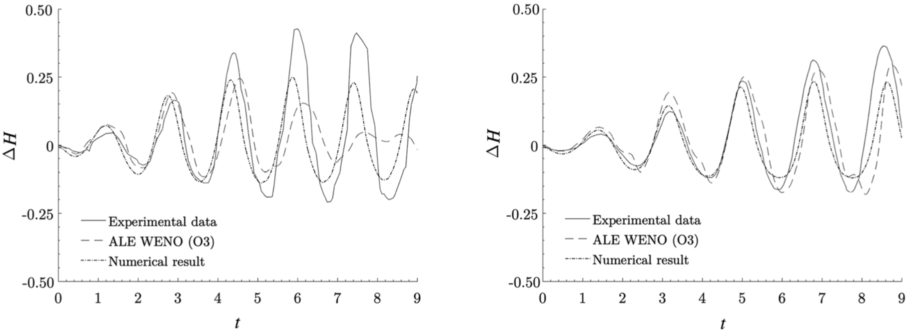

Fig. 15 Comparison for the sloshing in a moving tank test between the computed numerical solution, the experimental data provided by Faltinsen et al. [29] and the numerical results of Dumbser and Boscheri [25]. For the second pair of parameters $T = 1.5$ and $h_w = 0.6$ and the last pair $T = 1.875$ and $h_w = 0.5$

prescribed velocity is considered. Indeed, the water entry of a solid through the free surface is also a widely investigated field in the literature, since the knowledge of the pressure field acting on objects is a fundamental criterion for their design. In addition, being able to evaluate the pressure field acting on an object with sufficient accuracy could, in future method development, allow the dynamics of the solid phase to be evaluated directly, rather than imposing an a priori kinematic law. As for the sloshing phenomena studied in the previous section, the water entry of a two-dimensional symmetric wedge has been investigated both through analytical studies and numerical simulations, which are validated by comparing with experimental data, see e.g., the experiment which has been carried out by Zhao et al. [59] and the SPH method of Oger et al. [40]. Actually, this test case of a symmetric wedge impacting the free surface, refers to the experiment carried out by Zhao et al. [59], for which the motion of the wedge, i.e., the solid phase, was experimentally recorded and reported in Fig. 16.

The resulting flow and the solid-liquid interaction in general are even more complex in this test than in the previous one. Here, the wedge impact against calm water generates a large free surface deformation, which is followed by the formation of two jets running out along the edges of the wedge. An important feature is that the flow separates in a fixed separation point, which corresponds to the end of the edge, and it can be shown that the flow leaves the edge tangentially in the initial stages of the flow separation.

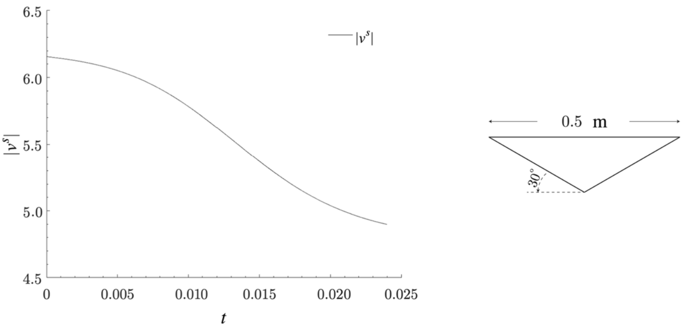

Fig. 16 The vertical drop velocity of the wedge recorded experimentally and the geometry of the wedge section having a deadrise angle of 30°

Then, at later stages it will no longer be a jet, the gravity will start to play a role and as the wedge penetrates the liquid the flow separation will also no longer be tangent to the edge. Considering pressure, as the wedge enters the water the maximum pressure will be located along the side at the highest wetted point, whereas after the flow separates, the pressure value near the separation point drops rapidly and the maximum pressure moves towards the bottom of the wedge. It is expected that the numerical method will be able to reproduce these resulting flow characteristics qualitatively. The computational domain is taken large enough to include the experimental material used for the laboratory measurements carried out by Zhao et al. [59], thus the domain is taken equal to $\Omega = [-0.5; 0.5] \times [-0.5; 0.5]$. The initial conditions for each phase, according to the geometry of the experimental section, which consider a wedge with a dead-rise angle of 30° illustrated in Fig. 16, are given by

$$\alpha^l(x, y, 0) = \begin{cases} 1, & \text{if } y \leqslant 0, \\ 1\mathrm{e}^{-2}, & \text{otherwise,} \end{cases} \tag{89}$$

$$\begin{aligned} &\alpha^s(x, y, 0) = \begin{cases} 1 - 1\mathrm{e}^{-2}, & \text{if } |x| \leqslant 0.25 \ \wedge \ y \geqslant \left| x \tan\left(\frac{\pi}{6}\right)\right| \ \wedge \ y \leqslant 0.25 \tan\left(\frac{\pi}{6}\right), \\ 0, & \text{otherwise,} \end{cases} \\ &p(x, y, 0) = \beta\left(\frac{2\,\alpha^l}{1 - \alpha^s} - 1\right), \qquad u_i^s(x, y, 0) = 0, \qquad u_i(x, y, 0) = 0, \end{aligned} \tag{90}$$

therefore, the fluid is set to be initially at rest while the wedge is entering the water free surface with an initial vertical velocity of $v^s(x, y, 0)$ =6.15 m/s. In this test, the motion of the wedge, i.e., the motion of the solid phase, is the drop velocity experimentally recorded by Zhao et al. [59] and reported in Fig. 16. The domain is discretized with 720 × 800 rectangular elements and periodic boundaries condition are set. The kinematic viscosity is assumed to be $\nu = 10^{-6}$. The numerical results, for this impact test, are represented in Fig. 17. From the top to the bottom results for three different instants are shown, namely for $t = 0.004\,37$ s, $t = 0.015\,8$ s, and $t = 0.020\,21$ s. From the left to the right, the liquid volume fraction α_l, the pressure field p, and a comparison with the analytical local pressure profile along the wedge boundary of Zhao et al. [59] are shown. The free-surface evolution, during the water entry of a wedge, illustrated in Fig. 17 on the left, shows quite well

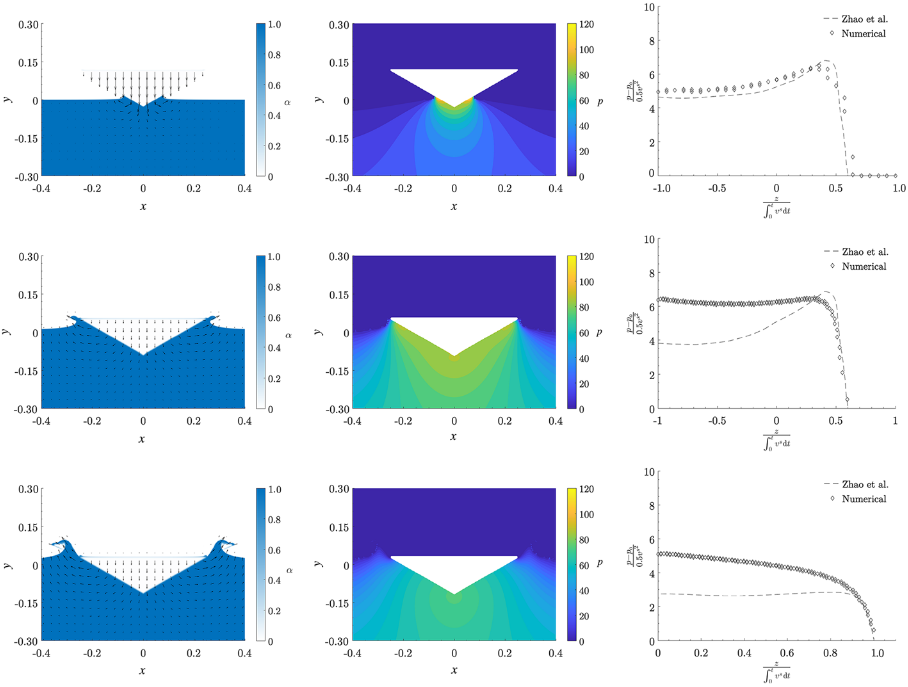

Fig. 17 From the left to the right, the liquid volume fraction α_l, the pressure field p, and a comparison with the analytical local pressure profile along the wedge boundary of Zhao et al. [59] are shown. From the top to the bottom results for three different instants are shown, namely for $t = 0.004\,3$ s, $t = 0.015\,8$ s, and $t = 0.020\,2$ s

the formation of two jets running out along the edges of the wedge. At time $t = 0.015\,8$ these two jets reach the separation point, which corresponds to the end of the edge. It can be seen that the flow leaves the edge tangentially at this initial stage of flow separation. Then, at $t = 0.020\,2$ it is possible to see that the flow separation is no longer tangent to the edge and a sort of breaking wave is developed. This shape of the jet is substantially different from the one obtained through the SPH method of Oger et al. [40], however, it is qualitatively similar to the experimental illustration given in the article of Zhao et al. [59]. Considering instead the pressure evolution, represented at the center of Fig. 17 it is possible to observe how the numerical method presented in this article succeeds in evaluating a much more uniform, symmetrical, and smooth pressure field than the one obtained with the SPH method of Oger et al. [40]. Furthermore, unlike SPH methods, where the estimation of the pressure field is a complex procedure, mainly in near boundary areas, in this pressure-based scheme the pressure field is obtained as directly and naturally as possible, in every part of the domain. A comparison is shown in the right-hand column of Fig. 17 with Zhao's analytical results, represented with a dashed line. The notation is the same as the one used in the article of Zhao et al. [59], p denotes the local pressure, p_o is the reference pressure assumed to be equal to β, $v^s(t)$ is the vertical velocity of the solid phase, z is the vertical coordinate on the wedge edge, z_k the vertical coordinate of the keel, and z_d of the highest part of the solid phase. With respect to the first instant $t = 0.004\,3$, the pressure profile along the edge is in good agreement with Zhao's analytical ones, then for later time frames the numerical results over-estimate the pressure values especially in the lower part of the wedge. However, the values are still qualitatively comparable. As the wedge enters into the water the maximum pressure values are located along the side at the highest wetted point, whereas after the flow separates, the pressure value near the separation point drops rapidly and the maximum pressure moves towards the bottom of the wedge.

5 Conclusions

In this paper, we have presented a semi-implicit mass and momentum conservative scheme for complex non-hydrostatic free surface flows, extending previous work on the subject presented in [18, 34]. Whereas in previous publications the solid phase was either absent or only fixed and while no physical viscosity was considered, in this paper a simplified Baer-Nunziato-type model in the incompressible limit is considered for viscous incompressible two-phase flows containing a liquid, a moving solid phase, and surrounding void. According to the diffuse interface approach, the domain is covered by the liquid phase, the solid phase, and the surrounding void via a scalar volume fraction function for each phase. Furthermore, a simplified interphase velocity relaxation source term is considered. It has been introduced to ensure that the boundary conditions between the two phases are automatically well imposed by solving the PDE.

In our numerical scheme, the dynamics of the liquid phase and the solid phase motion are decoupled. By solving the solid advection equation on a refined subgrid one obtains a sharp resolution of the new solid volume fraction distribution. Then, to solve the liquid phase related subsystems, which can be obtained from the flux splitting approach, a specific combination of explicit and implicit FV discretizations on staggered Cartesian control volumes is introduced, where the non-conservative products are treated by a path-conservative approach. The resulting semi-implicit FV discretization of the mass and momentum equations leads to a mildly nonlinear system for the pressure which can be efficiently solved with the nested Newton-type technique recently introduced and analyzed by Casulli et al. in [9, 10, 20, 21]. Last but not least, the time step size is only limited by the velocities of the two phases contained in the domain, and not by the gravity wave speed nor by the algebraic relaxation source term, which may also become stiff and thus requires an implicit discretization.

The resulting semi-implicit algorithm is first validated on a set of several academic classical Navier-Stokes problems further complicated by the addition of the solid phase, such as the Blasius boundary layer, Hagen-Poiseuille, and lid-driven cavity flows and was compared with existing exact or numerical reference solutions. In all these tests, good agreement was obtained between the numerical results and the reference solutions. Furthermore, some rather challenging computational results are shown for two-phase flow problems, such as free-surface flows which interact with moving solid bodies. For these tests the numerical results are validated by comparing with experimental and numerical results, which again are qualitatively in agreement. Last but not least, both in the viscous flow on a circular cylinder and in the water entry of a wedge tests the resulting pressure field acting on the solid phase is computed and reported and seems to be in agreement with the experimental reference solution. Thanks to this capability, in the future, the dynamics of the solid phase could be evaluated directly, rather than imposing an a priori kinematic law. Moreover, further work will concern the extension of this new numerical method also to more realistic and more complex three-dimensional two-phase flows and moving *elastic* solids, to the fully compressible case at all Mach numbers, see e.g., [6, 8, 26, 38, 42, 54, 55], and also to thermodynamically compatible discretizations, such as those recently forwarded in [1, 11, 53].

Acknowledgements This research was funded by the Italian Ministry of Education, University and Research (MIUR) in the frame of the Departments of Excellence Initiative 2018–2027 attributed to DICAM of the University of Trento (grant L. 232/2016), in the frame of the PRIN 2017 project *Innovative numerical methods for evolutionary partial differential equations and applications*, the PRIN 2022 project *High order structure-preserving semi-implicit schemes for hyperbolic equations*. D. is member of INdAM GNCS and was also co-funded by the European Union NextGenerationEU (PNRR, Spoke 7 CN HPC). Views and opinions expressed are however those of the author(s) only and do not necessarily reflect those of the European Union or the European Research Council. Neither the European Union nor the granting authority can be held responsible for them.

Funding Open access funding provided by Università degli Studi di Trento within the CRUI-CARE Agreement.

Data Availability The data can be obtained from the authors on reasonable request.

Declarations

Conflict of Interest The authors declare that they have no conflict of interest.

Ethical Standards The authors declare that they have complied with the commonly accepted ethical standards on Good Scientific Practice to the best of their knowledge. All funding sources have been declared in the previous Acknowledgments section.

Humans/Animals Rights This work concerns basic research in applied mathematics and does not involve any experiments on humans or animals, hence no ethical approval was needed for this research.

References

1. Abgrall, R., Busto, S., Dumbser, M.: A simple and general framework for the construction of thermodynamically compatible schemes for computational fluid and solid mechanics. Appl. Math. Comput. **440**, 127629 (2023)
2. Andrianov, N., Warnecke, G.: The Riemann problem for the Baer-Nunziato two-phase flow model. J. Comput. Phys. **212**, 434–464 (2004)
3. Baer, M.R., Nunziato, J.W.: A two-phase mixture theory for the deflagration-to-detonation transition (DDT) in reactive granular materials. J. Multiph. Flow **12**, 861–889 (1986)
4. Bermúdez, A., Busto, S., Dumbser, M., Ferrín, J., Saavedra, L., Vázquez-Cendón, M.: A staggered semi-implicit hybrid FV/FE projection method for weakly compressible flows. J. Comput. Phys. **421**, 109743 (2020)
5. Blasius, H.: Grenzschichten in Flüssigkeiten mit kleiner Reibung. Z. Math. Physik **56**, 1–37 (1908)

6. Boscheri, W., Dimarco, G., Loubère, R., Tavelli, M., Vignal, M.H.: A second order all Mach number IMEX finite volume solver for the three dimensional Euler equations. J. Comput. Phys. **415**, 109486 (2020)
7. Boscheri, W., Dumbser, M., Ioriatti, M., Peshkov, I., Romenski, E.: A structure-preserving staggered semi-implicit finite volume scheme for continuum mechanics. J. Comput. Phys. **2021**, 109866 (2010)
8. Boscheri, W., Pareschi, L.: High order pressure-based semi-implicit IMEX schemes for the 3D Navier-Stokes equations at all Mach numbers. J. Comput. Phys. **434**, 110206 (2021)
9. Brugnano, L., Casulli, V.: Iterative solution of piecewise linear systems. SIAM J. Sci. Comput. **30**, 463–472 (2007)
10. Brugnano, L., Casulli, V.: Iterative solution of piecewise linear systems and applications to flows in porous media. SIAM J. Sci. Comput. **31**, 1858–1873 (2009)
11. Busto, S., Dumbser, M.: A new class of simple, general and efficient finite volume schemes for overdetermined thermodynamically compatible hyperbolic systems. Commun. Appl. Math. Comput. (2023). https://doi.org/10.1007/s42967-023-00307-4
12. Busto, S., Dumbser, M., Río-Martín, L.: Staggered semi-implicit hybrid finite volume/finite element schemes for turbulent and non-Newtonian flows. Mathematics **9**, 2972 (2021)
13. Busto, S., Dumbser, M., Río-Martín, L.: An arbitrary-Lagrangian-Eulerian hybrid finite volume/finite element method on moving unstructured meshes for the Navier-Stokes equations. Appl. Math. Comput. **437**, 127539 (2023)
14. Busto, S., Ferrín, J.L., Toro, E.F., Vázquez-Cendón, M.E.: A projection hybrid high order finite volume/finite element method for incompressible turbulent flows. J. Comput. Phys. **353**, 169–192 (2018)
15. Busto, S., Río-Martín, L., Vázquez-Cendón, M., Dumbser, M.: A semi-implicit hybrid finite volume/finite element scheme for all Mach number flows on staggered unstructured meshes. Appl. Math. Comput. **402**, 126117 (2021)
16. Castro, M.J., Gallardo, J.M., Parés, C.: High-order finite volume schemes based on reconstruction of states for solving hyperbolic systems with nonconservative products. Applications to shallow-water systems. Math. Comput. **75**, 1103–1134 (2006)
17. Casulli, V.: A semi-implicit finite difference method for non-hydrostatic free-surface flows. Int. J. Numer. Methods Fluids **30**, 425–440 (1999)
18. Casulli, V.: A semi-implicit numerical method for the free-surface Navier-Stokes equations. Int. J. Numer. Methods Fluids **74**, 605–622 (2014)
19. Casulli, V., Stelling, G.S.: Semi-implicit subgrid modelling of three-dimensional free-surface flows. Int. J. Numer. Methods Fluids **67**, 441–449 (2011)
20. Casulli, V., Zanolli, P.: A nested Newton-type algorithm for finite volume methods solving Richards' equation in mixed form. SIAM J. Sci. Comput. **32**, 2255–2273 (2009)
21. Casulli, V., Zanolli, P.: Iterative solutions of mildly nonlinear systems. J. Comput. Appl. Math. **236**, 3937–3947 (2012)
22. Chiocchetti, S., Dumbser, M.: An exactly curl-free staggered semi-implicit finite volume scheme for a first order hyperbolic model of viscous flow with surface tension. J. Sci. Comput. **94**, 24 (2023)
23. Dumbser, M.: A simple two-phase method for the simulation of complex free surface flows. Comput. Methods Appl. Mech. Eng. **200**, 1204–1219 (2011)
24. Dumbser, M., Balsara, D., Tavelli, M., Fambri, F.: A divergence-free semi-implicit finite volume scheme for ideal, viscous and resistive magnetohydrodynamics. Int. J. Numer. Methods Fluids **89**, 16–42 (2019)
25. Dumbser, M., Boscheri, W.: High-order unstructured Lagrangian one-step WENO finite volume schemes for non-conservative hyperbolic systems: applications to compressible multi-phase flows. Comput. Fluids **86**, 405–432 (2013)
26. Dumbser, M., Casulli, V.: A conservative, weakly nonlinear semi-implicit finite volume method for the compressible Navier-Stokes equations with general equation of state. Appl. Math. Comput. **272**, 479–497 (2016)
27. Dumbser, M., Hidalgo, A., Castro, M., Parés, C., Toro, E.F.: Force schemes on unstructured meshes II: non-conservative hyperbolic systems. Comput. Methods Appl. Mech. Eng. **199**, 625–647 (2010)
28. Dumbser, M., Zanotti, O., Loubère, R., Diot, S.: A posteriori subcell limiting of the discontinuous Galerkin finite element method for hyperbolic conservation laws. J. Comput. Phys. **278**, 47–75 (2014)
29. Faltinsen, O., Rognebakke, O., Lukovsky, I., Timokha, A.: Adaptive multimodal approach to nonlinear sloshing in a rectangular tank. J. Fluid Mech. **407**, 201–234 (2000)
30. Fambri, F., Dumbser, M.: Spectral semi-implicit and space-time discontinuous Galerkin methods for the incompressible Navier-Stokes equations on staggered Cartesian grids. Appl. Numer. Math. **110**, 41–74 (2016)

31. Fambri, F., Dumbser, M.: Semi-implicit discontinuous Galerkin methods for the incompressible Navier-Stokes equations on adaptive staggered Cartesian grids. Comput. Methods Appl. Mech. Eng. **324**, 170–203. arXiv:1612.09558 (2017)
32. Favrie, N., Gavrilyuk, S.: Diffuse interface model for compressible fluid-compressible elastic-plastic solid interaction. J. Comput. Phys. **231**, 2695–2723 (2012)
33. Favrie, N., Gavrilyuk, S., Saurel, R.: Solid-fluid diffuse interface model in cases of extreme deformations. J. Comput. Phys. **228**, 6037–6077 (2009)
34. Ferrari, D., Dumbser, M.: A mass and momentum-conservative semi-implicit finite volume scheme for complex nonhydrostatic free surface flows. Int. J. Numer. Methods Fluids **93**, 2946–2967 (2021)
35. Gaburro, E., Castro, M., Dumbser, M.: A well balanced diffuse interface method for complex nonhydrostatic free surface flows. Comput. Fluids **175**, 180–198 (2018)
36. Ghia, U., Ghia, K.N., Shin, C.T.: High-*Re* solutions for incompressible flow using Navier-Stokes equations and multigrid method. J. Comput. Phys. **48**, 387–411 (1982)
37. Kemm, F., Gaburro, E., Thein, F., Dumbser, M.: A simple diffuse interface approach for compressible flows around moving solids of arbitrary shape based on a reduced Baer-Nunziato model. Comput. Fluids **204**, 104536 (2020)
38. Lukácová-Medvidóvá, M., Puppo, G., Thomann, A.: An all Mach number finite volume method for isentropic two-phase flow. J. Numer. Math. **31**, 175–204 (2023)
39. Ndanou, S., Favrie, N., Gavrilyuk, S.: Multi-solid and multi-fluid diffuse interface model: applications to dynamic fracture and fragmentation. J. Comput. Phys. **295**, 523–555 (2015)
40. Oger, G., Doring, M., Alessandrini, B., Ferrant, P.: Two-dimensional SPH simulations of wedge water entries. J. Comput. Phys. **213**, 803–822 (2006)
41. Parés, C.: Numerical methods for nonconservative hyperbolic systems: a theoretical framework. SIAM J. Numer. Anal. **44**, 300–321 (2006)
42. Park, J., Munz, C.: Multiple pressure variables methods for fluid flow at all Mach numbers. Int. J. Numer. Methods Fluids **49**, 905–931 (2005)
43. Prandtl, L.: Über Flüssigkeitsbewegung bei sehr kleiner Reibung. In: Verhandlg. III. Intern. Math. Kongr. Heidelberg, pp. 484–491 (1904)
44. Re, B., Abgrall, R.: A pressure-based method for weakly compressible two-phase flows under a Baer-Nunziato type model with generic equations of state and pressure and velocity disequilibrium. Int. J. Numer. Methods Fluids **94**, 1183–1232 (2022)
45. Saurel, R., Abgrall, R.: A multiphase Godunov method for compressible multifluid and multiphase flows. J. Comput. Phys. **150**, 425–467 (1999)
46. Schlichting, H., Gersten, K.: Grenzschicht-Theorie. Springer, Berlin, Heidelberg (2006)
47. Schwendeman, D.W., Wahle, C.W., Kapila, A.K.: The Riemann problem and a high-resolution Godunov method for a model of compressible two-phase flow. J. Comput. Phys. **212**, 490–526 (2006)
48. Shao, J., Li, H., Liu, G., Liu, M.: An improved SPH method for modeling liquid sloshing dynamics. Comput. Struct. **100/101**, 18–26 (2012)
49. Tavelli, M., Dumbser, M.: A staggered semi-implicit discontinuous Galerkin method for the two dimensional incompressible Navier-Stokes equations. Appl. Math. Comput. **248**, 70–92 (2014)
50. Tavelli, M., Dumbser, M.: A staggered space-time discontinuous Galerkin method for the three-dimensional incompressible Navier-Stokes equations on unstructured tetrahedral meshes. J. Comput. Phys. **319**, 294–323 (2016)
51. Tavelli, M., Dumbser, M.: A pressure-based semi-implicit space-time discontinuous Galerkin method on staggered unstructured meshes for the solution of the compressible Navier-Stokes equations at all Mach numbers. J. Comput. Phys. **341**, 341–376 (2017)
52. Tavelli, M., Dumbser, M.: Arbitrary high order accurate space-time discontinuous Galerkin finite element schemes on staggered unstructured meshes for linear elasticity. J. Comput. Phys. **366**, 386–414 (2018)
53. Thomann, A., Dumbser, M.: Thermodynamically compatible discretization of a compressible two-fluid model with two entropy inequalities. J. Sci. Comput. **97**, 9 (2023)
54. Thomann, A., Puppo, G., Klingenberg, C.: An all speed second order well-balanced IMEX relaxation scheme for the Euler equations with gravity. J. Comput. Phys. **420**, 109723 (2020)
55. Thomann, A., Zenk, M., Puppo, G., Klingenberg, C.: An all speed second order IMEX relaxation scheme for the Euler equations. Commun. Comput. Phys. **28**, 591–620 (2020)
56. Toro, E.F.: Riemann Solvers and Numerical Methods for Fluid Dynamics. Springer, Berlin (2009)
57. Toro, E.F., Vázquez-Cendón, M.E.: Flux splitting schemes for the Euler equations. Comput. Fluids **70**, 1–12 (2012)
58. Williamson, C., Brown, G.L.: A series in $1/Re$ to represent the Strouhal-Reynolds number relationship of the cylinder wake. J. Fluids Struct. **12**, 1073–1089 (1998)

59. Zhao, R., Faltinsen, O., Aarsnes, J.: Water entry of arbitrary two-dimensional sections with and without flow separation. In: Proceedings of the 21st Symposium on Naval Hydrodynamics (1997)

Authors and Affiliations

Davide Ferrari[1] · **Michael Dumbser**[1]

✉ Michael Dumbser
michael.dumbser@unitn.it

Davide Ferrari
davide.ferrari@unitn.it

[1] Department of Civil, Environmental and Mechanical Engineering, University of Trento, Via Mesiano 77, 38123 Trento, Italy